IMAGING OF METAL SURFACES USING CONFOCAL LASER SCANNING
MICROSCOPY

THESIS SUBMITTED TO
THE GRADUATE SCHOOL OF NATURAL AND APPLIED SCIENCES
OF
MIDDLE EAST TECHNICAL UNIVERSITY

BY

BİLGE CAN YILDIZ

IN PARTIAL FULFILLMENT OF THE REQUIREMENTS
FOR
THE DEGREE OF MASTER OF SCIENCE
IN
PHYSICS

SEPTEMBER 2011

Approval of the thesis:

**IMAGING OF METAL SURFACES USING
CONFOCAL LASER SCANNING MICROSCOPY**

submitted by **BİLGE CAN YILDIZ** in partial fulfillment of the requirements for the
degree of **Master of Science in Physics, Middle East Technical University** by,

Prof. Dr. Canan Özgen
Dean, Graduate School of **Natural and Applied Sciences**   _____

Prof. Dr. Sinan Bilikmen
Head of Department, **Physics**   _____

Assist. Prof. Dr. Hakan Altan
Supervisor, **Physics, METU**   _____

Examining Committee Members:

Assoc. Prof. Dr. Serhat Çakır
Physics, METU   _____

Assist. Prof. Dr. Hakan Altan
Physics, METU   _____

Assist. Prof. Dr. Alpan Bek
Physics, METU   _____

Assoc. Prof. Dr. Akif Esendemir
Physics, METU   _____

Assist. Prof. Dr. Behzat Şahin
Electrical and Electronics Engineering, METU   _____

                    Date: _____

I hereby declare that all information in this document has been obtained and presented in accordance with academic rules and ethical conduct. I also declare that, as required by these rules and conduct, I have fully cited and referenced all material and results that are not original to this work.

Name, Last name: Bilge Can Yıldız

Signature:

ABSTRACT

IMAGING OF METAL SURFACES USING CONFOCAL LASER SCANNING MICROSCOPY

Yıldız, Bilge Can

M.Sc., Department of Physics

Supervisor: Assist. Prof. Dr. Hakan Altan

September 2011, 75 pages

Optical imaging techniques have improved much over the last fifty years since the invention of the laser. With a high brightness source many imaging applications which were once inaccessible to researchers have now become a reality. Among these techniques, the most beneficial one is the use of lasers for both wide-field and confocal imaging systems.

The aim of this study was to design a laser imaging system based on the concept of laser scanning confocal microscopy. Specifically the optical system was based on optical fibers allowing the user to image remote areas such as the inner surface of rifled gun barrels and/or pipes with a high degree of precision (+/- 0.01 mm). In order to build such a system, initially the theoretical foundation for a confocal as well as a wide-field imaging system was analyzed. Using this basis a free-space optical confocal system was built and analyzed. The measurements support the fact that both the objective numerical aperture and pinhole size play an important role in the radial and axial resolution of the system as well as the quality of the images obtained.

To begin construction of a confocal, optical-fiber based imaging system first an all-fiber wide-field imaging system was designed and tested at a working wavelength of 1550 nm. Then an all fiber confocal system was designed at a working wavelength of 808 nm. In both cases results showed that while lateral resolution was adequate, axial resolution suffered since it was found that the design of the optical system needs to take into account under-filling of the objective lens, a result common with the use of laser beams whose divergence is not at all like that of a point source.

The work done here will aid technology that will be used in the elimination process of faulty rifling fabrication in defense industry. The reason why the confocal technique is preferred to the conventional wide-field one is the need for better resolution in all directions. Theoretical concepts and mathematical background are discussed as well as the experimental results and the practical advantages of such a system.

Keywords: Confocal-scanning laser microscope, wide-field imaging techniques, fiber optical imaging techniques

ÖZ

METAL YÜZEYLERİN EŞ-ODAKLI LAZER TARAMALI MİKROSKOP SİSTEMİ İLE GÖRÜNTÜLENMESİ

Yıldız, Bilge Can

Yüksek Lisans, Fizik Bölümü

Tez Yöneticisi: Yrd. Doç. Dr. Hakan Altan

Eylül 2011, 75 sayfa

Lazerin keşfinden bu yana, son elli yılda optik görüntüleme teknikleri oldukça gelişti. Daha önceleri araştırmacılar için ulaşılamaz olan yüksek parlaklıkta kaynaklarla yapılan birçok görüntüleme uygulaması bugün artık bir gerçeklik haline geldi. Bu teknikler arasında lazer, hem geleneksel hem de eş-odaklı görüntüleme sistemlerinde en faydalı olanıdır.

Bu çalışmanın amacı lazer taramalı eş-odaklı mikroskop kavramına dayanan bir lazer görüntüleme sistemi tasarlamaktır. Özel olarak, optik sistem, kullanıcıya yivli silah namlularının iç yüzeyleri gibi ulaşılması zor olan alanların yüksek hassasiyet ile (+/- 0.01 mm) görüntülenebilmesi için olanak tanıyan optik fiberler üzerine temellendirildi. Böyle bir sistemi kurmak için ilk olarak hem eş-odak hem de geleneksel görüntüleme sistemlerinin teorik esasları incelendi. Bu esaslara dayanılarak ışığın havada ilerlediği bir eş-odaklı optik sistem kuruldu ve incelendi. Ölçümler, elde edilen görüntülerin kalitesi kadar, radyal ve eksensel çözünürlüklerde de hem objektifin sayısal açıklığının hem de iğne deliği büyüklüğünün önemli bir rol oynadığı gerçeğini destekledi.

Optik-fiber temelli, eş-odaklı görüntüleme sisteminin kurulumuna başlamadan önce, ilk olarak 1550 nm dalgaboyunda çalışan, bütünüyle fiber temelli bir geleneksel görüntüleme sistemi tasarlandı ve test edildi. Daha sonra, 808 nm dalgaboyunda çalışan, bütünüyle fiber temelli bir eş-odaklı sistem tasarlandı. Her iki sistemde de sonuçlar, radyal çözünürlüğün yeterli olduğunu fakat eksensel çözünürlüğün, ıraksaklığı noktasal kaynaklarınki gibi olmayan lazer ışınının kullanılmasının yaygın bir sonucu olan, objektif merceğin ışın tarafından tam olarak doldurulmayacağının göz önüne alınması gerekliliği ortaya çıktığı için istenilen düzeyde olmadığını gösterdi.

Bu çalışma savunma sanayisinde hatalı üretilen namlu yiv setlerinin elenmesi sürecinde kullanılacak teknolojiye destek olacaktır. Geleneksel yaygın görüntüleme tekniği yerine eş-odaklı görüntüleme tekniğinin tercih edilmesinin sebebi her yönde iyi çözünürlük elde etme ihtiyacıdır. Böyle bir sistemin pratik üstünlükleri ve deneysel sonuçlar yanı sıra teorik ve matematiksel arka plan da tartışılmıştır.

Anahtar Kelimeler: Eş-odaklı lazer taramalı mikroskop, geleneksel görüntüleme teknikleri, fiber optik görüntüleme teknikleri

To my family

ACKNOWLEDGEMENTS

TABLE OF CONTENTS

LIST OF FIGURES

CHAPTER 1

INTRODUCTION

Various metals and metal parts are used in manufacturing and machine technologies. These range from aluminum and steel to precious metals such as gold and platinum. As the metals are processed to obtain various machine parts (such as rifled bores) or pieces they can display various defects which may or may not affect their performance. The elimination process of faulty fabricated products is one of the vital issues particularly in the defense industry. While processing these metal raw materials, the imperfections may result on the surfaces, amounts of which affect the quality of products such as rifled gun barrels. Rifled gun barrels typically use steel as a raw material. This raw material is molded and shaped through many industrial processes such as melting, cooling, milling, drilling and polishing. All of these processes can affect the quality of the gun barrel. For the improvement of manufacture and quality control, it is imperative that these surface defects can be characterized.

Rifling is the process of forming grooves inside a barrel of a gun. This helical form of the barrel make the bullets spin inside the gun bore to obtain a stabilized projectile motion. Accurate rifling is characterized by its twist rate, distance of which the bullet completes one full revolution [1]. Defects on the surface of a rifled gun barrel affect its performance therefore detection of these defects is very important to improve manufacture and quality control.

Low-quality products result in much more critical problems in the defense industry than any other industrial area. That is why the detection of these defects, i.e., an effective elimination process of faulty fabricated products, is very important for the quality sustainability and development of defense industry.

Technologies based on magnification/eye imaging using endoscopic systems have been traditionally used to detect defects, such as bumps, burrs, marks and holes. For the detection of imperfections on the surface of gun barrels, the traditional methods of imaging were based on the borescope-fiberscobe technique. Borescope was discovered by a British physicist of applied optics, Harold Hopkins in early 1950's [2]. His invention was invaluable for the reason that it is still used commonly in visual inspection of inaccessible areas of many kinds of objects in a variety of industrial, scientific or any research areas. Hopkins' first invention was the zoom-lens which gained television images a revolutionary improvement [3]. At late 1950's and early 1960's, the outputs of Hopkins' studies, fiberscope-borescope and rod-lens endoscope techniques resulted in improvements in medical surgery as well as various industrial areas.
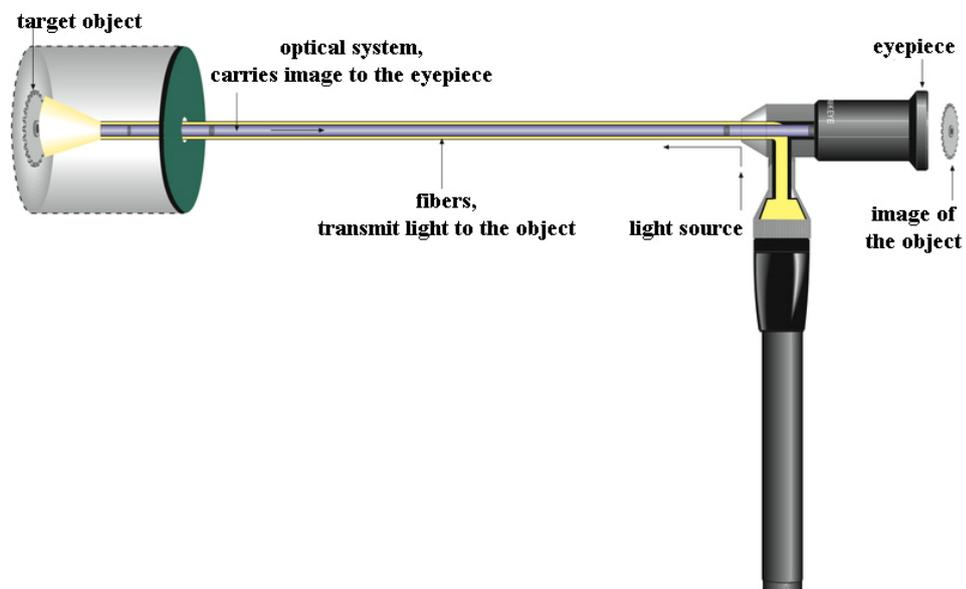
Figure 1.1 A schematic view of a typical borescope

A borescope images the viewing area of a sample with an objective lens, and then the formed image is transferred to an eyepiece placed on one end by an optical system including variety of lenses along a rod (bore) [4]. A fiberscope is very similar to a borescope except fiberscopes are made up of bundles of fiber optic cables, they are flexible and therefore they can be curled into otherwise inaccessible areas. Figure 1.1 shows a typical rigid borescope.

This technique is able to provide an image resolution about 50-100 microns which is the limit of the resolution of a human eye. However, imperfections and cracks below this limit affect the performance of the gun barrel. In order to have an effective elimination process of faulty rifling fabrication, which is very crucial in defense industry, it is important to be able to image the surface of the gun barrel below this resolution limit.
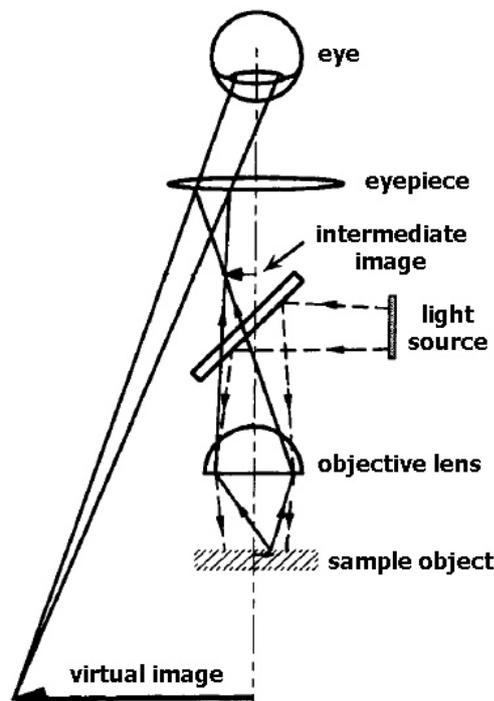
Figure 1.2 A schematic of a conventional microscope

Furthermore, borescope techniques lack of ability to display three dimensional images. Inanc, in his study, "A borescope based optical surface scanner", was able to scan a 2.5 cm x 3.5 cm strip in 5 minutes, however, for some sharp height variations, there was unreliable data, which corresponds to a bad sense of depth [5].

Borescope techniques are based on conventional wide field microscopy. The working principle in a standard microscopy is that the light source illuminates the sample through an objective lens, objective lens forms a real inverted image in the intermediate plane of microscope. This image is, then, viewed through the eyepiece to form a much more magnified virtual image at a reasonable distance from the eye [6]. Figure 1.2 shows a simplified schematic of a standard microscope.

A standard microscope may be a reasonable choice for a need to image thin samples. A sample with 1 or 2 μm width is considered as two dimensional and all points of this sample lie on the same focal plane. Image of such a sample may be satisfactory for many research areas [7]. However, when a thick object is imaged by conventional microscope, both focal and out-of-focus points are reflected to one image plane, i.e., a three dimensional object is projected as an image to a two dimensional image plane.

Since the out-of-focus points are included to the image formation, by using conventional standard microscope, it is not possible to detect defects on a metal surface properly. Confocal microscopy technique eliminates defocus plane by a pinhole, therefore instead of blurring of defocus points, collects serial cross sections, and provides high contrast three dimensional images [8]. That is why the confocal technique is a better choice instead of wide field techniques for imaging surfaces of rifled gun barrels.

Confocal microscopy is an optical imaging technique with an essential advantage of providing three dimensional images with high resolution [9]. A confocal microscope basically works as it scans the target object surface point by point, by focusing the light coming from the target object onto a spatial pinhole eliminating the out of focus light, providing higher resolution and contrast in the direction of optical axis [10].

Figure 1.3 shows a basic scheme of a confocal scanning optical microscope. In Figure 1.3.a., one spot of the sample is illuminated at a time and the light reflected back from the sample (in this case from the focal plane) comes out of the pinhole and imaged by a photo-detector behind the pinhole. Scanning the sample point by point in this way forms a complete image as a combination of all illuminated points. If a point on the sample is out of focus (a tiny hole on the sample for instance), this time the reflected beam fails to pass thorough the pinhole, and is defocused on the image plane, as represented in Figure 1.3.b. This working principle provides high resolution in z-direction, thus one can obtain a three dimensional illustration of various samples [11].

a)

pinhole

illuminating beam

focal plane

b)

illuminating beam

pinhole

out-of-focus plane

focal plane

c)

signal from photodetector

movement in the direction of z
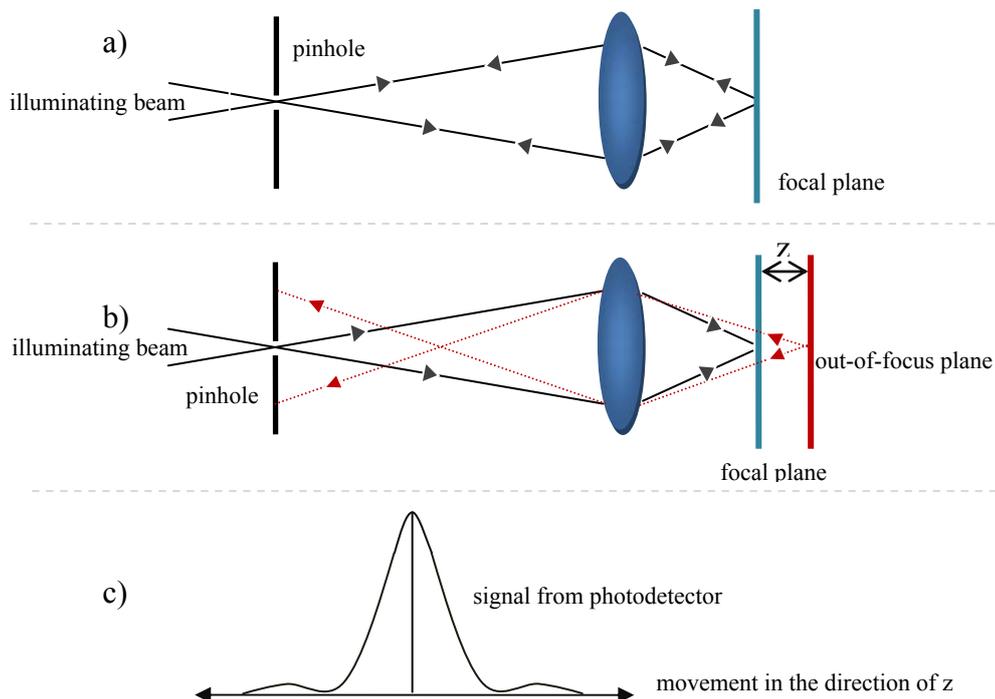
Figure 1.3 a) Focal plane of the sample, light (black) reflected back from the sample, succeeded in coming out of the pinhole b) out of focus plane, light (red) reflected back from the sample failed to come out of the pinhole c) the signal

The idea of a scanning microscope was first suggested by Young and Roberts in 1951 for biological imaging [12]. They used the scanning spot of a cathode ray tube as the light source and let the light propagate through conventional microscope optics to get an image of a spot on the sample. Their microscope was named as "the flying spot microscope" and displayed reasonable magnification, contrast and resolution values [13] [14], however, since the light was weak, their system suffered from signal-to-noise problems [12].

The idea of confocal microscopy was first created by Marvin Minsky, son of an ophthalmologist, in 1955 while he was a Junior Fellow at Harvard University. He studied mostly biological sciences and focused specifically on the structure of the human brain [12].

Minsky started from the idea that a well-functioning microscope had to check each and every point of a specimen and sense the amount of light scattered or absorbed by that single point. However, such measurements of points of specimens resulted in low-resolution images because trying to measure points simultaneously caused every focal image point to be blurred by aberrant rays scattered from some other points of the specimen. Therefore the measurement of a point should not contain the aberrant rays scattered from the out of interest points which will cause a cloudy focal image. Scanning the specimen surface and excluding the aberrant out-of-focus light by using a second lens to refocus the rays reflected back from the specimen onto a pinhole was a great solution to these deals, thereto made him procure a patent of his invention so called scanning confocal microscope [15].

One drawback of confocal scanning systems is that there are not many emitted photons to collect at any instant, and not to have noisy images, a point has to be illuminated for enough time, which increases the length of scanning time [16] [17]. The solution to this problem, however, is to use a source of very high intensity. Therefore the modern choice for the source of confocal scanning systems is lasers with additional benefit of being available in a wide range of wavelengths.

Laser has not been invented yet those days, so the weakness of the light was still an issue. The light sources used by Minsky are carbon arc and zirconium arc which were the brightest sources available those days [18] [15]. Although Minsky evidently explained the theoretical details of the way of image displaying mechanism of his invention in his patent, he had a mistake by using too much magnification, i.e. the scanning line was more closely spaced than the width of a single spot, resulting cloudy images [12].

The development of confocal microscopy started from the early 1950's and still continues, allowing improvements in speed, image quality, and digital storage of the generated images utilizing the advantage of optics and electronics.

In a confocal laser scanning microscope, where a laser illumination is used as a light source, light illuminating from the source is focused by an objective onto the target surface, then the reflected and scattered light from the surface is refocused but this time onto a pinhole behind which a photo detector collects the light that come out of the pinhole. In such a setup either the sample is stationary whereas the beam path is moved with couple of reflecting mirrors, as represented by the scheme in Figure 1.4, or the beam path determined by beam splitters is stationary whereas the sample is attached to a moving stage [19] [20]. The last method was preferred by Minsky as well as the creators of many modern systems, with the advantages of bringing minimum optical aberrations and provided that the whole field of view is illuminated uniformly [16].

With the advantage of providing three dimensional images with high resolutions in all directions, confocal microscopy is an important method in either scientific or industrial areas where imaging is a crucial part of the application. That is why confocal microscopy has been chosen as the basis of this study, among all the other techniques of imaging rifled gun barrels.
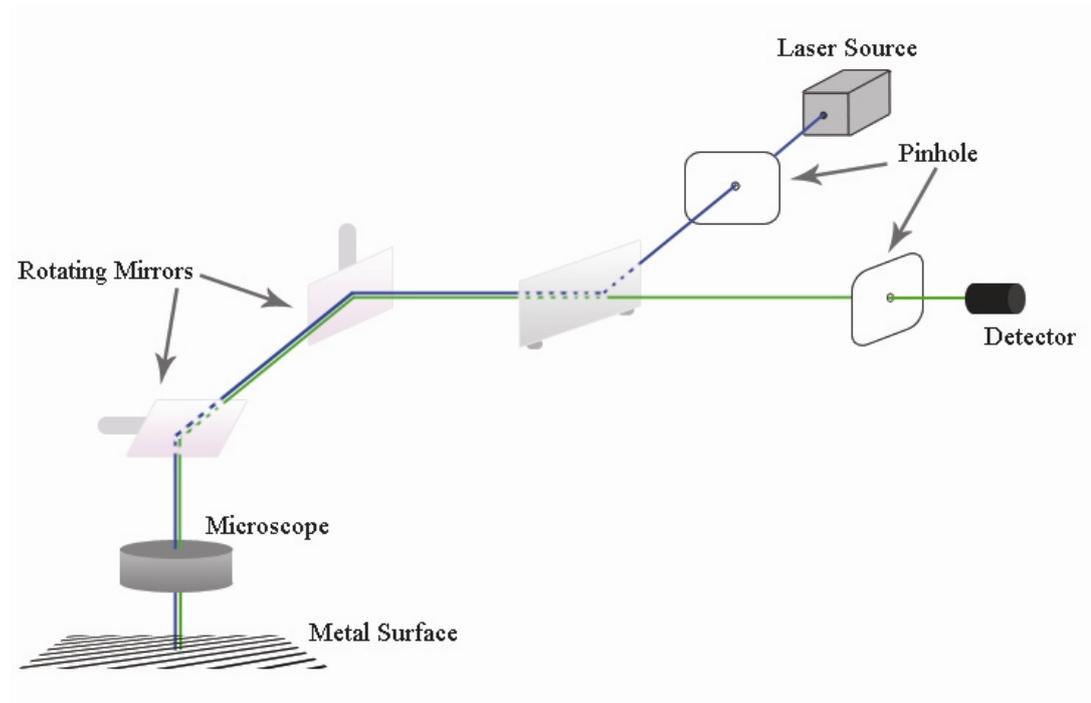
Figure 1.4 Basic setup of a laser scanning confocal microscope with a stationary target object method

This study aims to design a laser-based imaging system using fiber-optics to image the surfaces of the rifled gun barrels. Initially, a theoretical description of the imaging using wide field and confocal techniques are given. Theoretical limitations are discussed for specific cases and when using laser beams as an illumination source instead of point sources. Afterwards, confocal and wide-field imaging systems are designed and analyzed. For imaging rifled gun barrels, a final system is aimed to achieve an image in three-dimensions by using confocal techniques with a resolution value on the order of 0.01 mm. The objects to be measured are gun barrels with lengths 10-70 mm, and inner diameters 5.5-20 mm. In particular, diameters of gun barrels to be measured are 5.56; 7.62; 9.00 mm. That means the system has to be constructed by taking these specific parameters into account. That brings some limitations such as; the optical system has to be fit into an area having a diameter at

most ~5.5 mm, in accordance with the narrowest gun bore to be measured that is 5.56 mm. Further, since the widest gun bore to be measured has a diameter of 9 mm, the system has to be designed such that the objective lens can focus the laser beam ~4.5 mm away from itself. The details of the systems are given including these restrictions.

In Chapter 2, there is a detailed theoretical explanation of confocal microscopy with comparisons of point spread functions and resolution values of wide field and confocal systems. Chapter 3 includes the description of a home-built confocal microscope where the light propagates in the air. In chapter 4, the development of two fiber optic systems based on two different wavelengths is discussed, and one is a wide field system whereas the other is a confocal system. Chapter 5 includes the discussion and conclusions of the whole study.

CHAPTER 2

CONFOCAL MICROSCOPY – A THEORETICAL TREATISE

This chapter focuses on the theoretical background of confocal microscopy, starting from wide field microscopy, by utilizing the point spread function, intensity and resolution.

Point spread function (PSF) can be considered as a pattern of the image formed by an optical system. PSF defines the image since it is the energy distribution of the image with respect to the position. In this chapter, we will show that the PSF that is obtained using a confocal technique is much sharper than a PSF obtained using wide field techniques. Essentially, PSF of a confocal system is simply the square of the PSF of a usual optical system [21] [22].

2.1 The Field Vectors in the Image Space

In this section, the methodology laid out by Born and Wolf [23] is followed, where the electric and magnetic components of a point in the image is derived mathematically, and used to derive the energy density and finally point spread function of the optical system.

It is assumed that the system is an aplanatic optical system with a point source, assumed to be at infinity, in the direction of the optical axis. It is meant by an aplanatic system that it is free from both spherical aberration[1] and coma[2], and obeys

---

[1] A defect of lenses in which rays of light parallel to but far from the optical axis are brought to a different focus from those close to the axis. An image suffering from spherical aberration has no unique focus.

[2] A coma is defined as a variation in magnification over the entrance pupil in an optical system.

the Abbe sine condition[3]. The source is assumed to give rise to a linearly polarized monochromatic wave in the entrance pupil of the system, and it is also assumed that the linear dimensions of the exit pupil are large compared with wavelength.

Electric and magnetic field vectors at any point P(x, y, z) in the image space are given by the following [23];

$$\mathbf{E}(x,y,z,t) = \Re\left\{\mathbf{e}(x,y,z)e^{-i\omega t}\right\}, \qquad \mathbf{B}(x,y,z,t) = \Re\left\{\mathbf{h}(x,y,z)e^{-i\omega t}\right\} \tag{2.1.1}$$

where the vectors $\mathbf{e}$ and $\mathbf{h}$ are the time independent parts of the fields.

$$\mathbf{e}(x,y,z) = -\frac{ik}{2\pi}\iint_{\Omega}\frac{\mathbf{a}(s_x,s_y)}{s_z}\exp\left\{ik\left[\Phi(s_x,s_y)+s_x x+s_y y+s_z z\right]\right\}ds_x ds_y \tag{2.1.2}$$

$$\mathbf{h}(x,y,z) = -\frac{ik}{2\pi}\iint_{\Omega}\frac{\mathbf{b}(s_x,s_y)}{s_z}\exp\left\{ik\left[\Phi(s_x,s_y)+s_x x+s_y y+s_z z\right]\right\}ds_x ds_y \tag{2.1.3}$$

Here, $\mathbf{a}$ and $\mathbf{b}$ are the 'strength factors' of the unperturbed electromagnetic field which is incident on the exit pupil [23].

Φ is the aberration function of the system, which is equal to zero for aplanatic systems as in the problem under consideration. k is the vacuum wave number, which is equal to 2π divided by the wavelength, λ. s_x, s_y, and s_z are the components of the unit vector $\mathbf{s}$ which is in the direction of the ray in the image field, as seen in the Figure 2.1. And finally Ω is the solid angle formed by all the geometrical rays that pass through the exit pupil of the system.

---

[3] The Abbe sine condition is a condition that must be fulfilled by a lens or other optical system in order for it to produce sharp images of off-axis as well as on-axis objects.
The mathematical condition is as follows:

$$\frac{\sin u'}{\sin U'} = \frac{\sin u}{\sin U}$$

where the variables u, U are the angles (relative to the optic axis) of any two rays as they leave the object, and u', U' are the angles of the same rays where they reach the image plane.
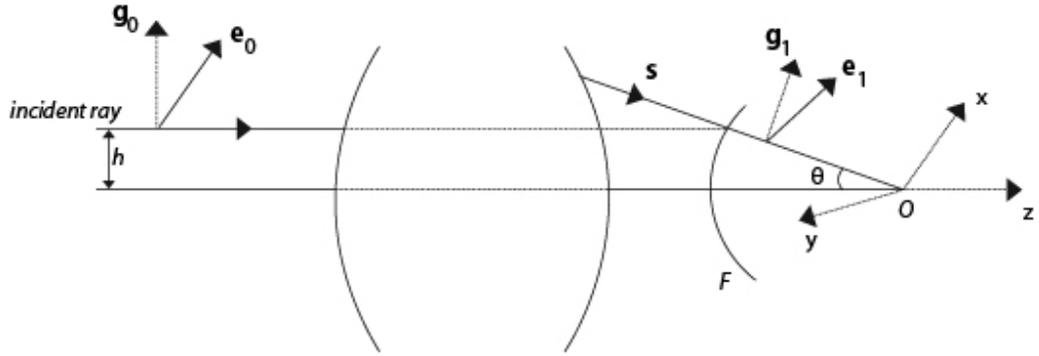
Figure 2.1 The meridional plane of ray

In Figure 2.1, F is the focal sphere with centre at point O and with radius f, equal to the focal length of the system. $\mathbf{e_0}$ is the electric field vector of the incident ray and it is in the direction of x axis. In order to determine $\mathbf{e_1}$, $\mathbf{g_0}$ and $\mathbf{g_1}$ are introduced such that $\mathbf{g_0}$ is perpendicular to the direction of the ray in the object plane and $\mathbf{g_1}$ is perpendicular to the direction of the ray in the image plane.

The relationship between the strength vectors and $\mathbf{s}$ is following [23];

$$\mathbf{b} = \mathbf{s} \times \mathbf{a} \qquad (2.1.4)$$

And $\mathbf{a}$ is defined as [23] ;

$$\mathbf{a} = f l_0 \cos^{\frac{1}{2}} \theta \hat{\mathbf{e}}_1 \qquad (2.1.5)$$

Where l_0 is the amplitude factor, f is the focal length and θ is the angle between the vector $\mathbf{s}$ and the axis of incident ray. Since electric and magnetic fields are orthogonal to the ray; $\mathbf{e_1}$ lies in the plane of $\mathbf{g_1}$ and $\mathbf{g_1}$ x $\mathbf{s}$, that is;

$$\mathbf{e_1} = \alpha \mathbf{g_1} + \beta (\mathbf{g_1} \times \mathbf{s}) \qquad (2.1.6)$$

12

where α and β are some constants. Using the fact that as the light traverses the system, the angle between the electric (and also magnetic) vector and the meridional plane of the ray remains constant, α and β are determined as the following;

$$\mathbf{g}_1 \cdot \hat{\mathbf{e}}_1 = \mathbf{g}_0 \cdot \mathbf{i}$$

$$(\mathbf{g}_1 \times \mathbf{s}) \cdot \hat{\mathbf{e}}_1 = (\mathbf{g}_0 \times \mathbf{k}) \cdot \mathbf{i} \tag{2.1.7}$$

Substituting from (2.1.6) into (2.1.7), it is found that;

$$\alpha = \mathbf{g}_0 \cdot \mathbf{i}, \qquad \beta = (\mathbf{g}_0 \times \mathbf{k}) \cdot \mathbf{i} = \mathbf{g}_0 \cdot (\mathbf{k} \times \mathbf{i}) = \mathbf{g}_0 \cdot \mathbf{j} \tag{2.1.8}$$

and from (2.1.5), (2.1.6) and (2.1.8), it follows that;

$$\mathbf{a} = fl_0 \sqrt{\cos\theta} \left[(\mathbf{g}_0 \cdot \mathbf{i})\mathbf{g}_1 + (\mathbf{g}_0 \cdot \mathbf{j})(\mathbf{g}_1 \times \mathbf{s}) \right] \tag{2.1.9}$$

It is convenient to rewrite the strength vectors in spherical polar coordinates; r, θ, φ, where;

$$s_x = \sin\theta\cos\phi, \; s_y = \sin\theta\sin\phi, \; s_z = \cos\theta; \qquad \mathbf{s} = s_x\mathbf{i} + s_y\mathbf{j} + s_z\mathbf{k} \tag{2.1.10}$$

For any point, in the image region P(x, y, z) can be written as;

$$x = r_P \sin\theta_P \cos\phi_P, \; y = r_P \sin\theta_P \sin\phi_P, \; z = r_P \cos\theta_P; \tag{2.1.11}$$

$s_x x + s_y y + s_z z$ can be written as;

$$
\begin{aligned}
s_x x &+ s_y y + s_z z \\
&= (\sin\theta\cos\phi)(r_P\sin\theta_P\cos\phi_P) + (\sin\theta\sin\phi)(r_P\sin\theta_P\sin\phi_P) + (\cos\theta)(r_P\cos\theta_P) \\
&= r_P \left[\sin\theta\sin\theta_P (\cos\phi\cos\phi_P + \sin\phi\sin\phi_P) + \cos\theta\cos\theta_P \right] \\
&= r_P \left[\sin\theta\sin\theta_P \cos(\phi - \phi_P) + \cos\theta\cos\theta_P \right] \\
&= r_P \cos\varepsilon
\end{aligned}
$$

where; (see Figure 2.2)

$$\cos\varepsilon = \cos\theta\cos\theta_P + \sin\theta\sin\theta_P\cos(\phi - \phi_P) \tag{2.1.12}$$
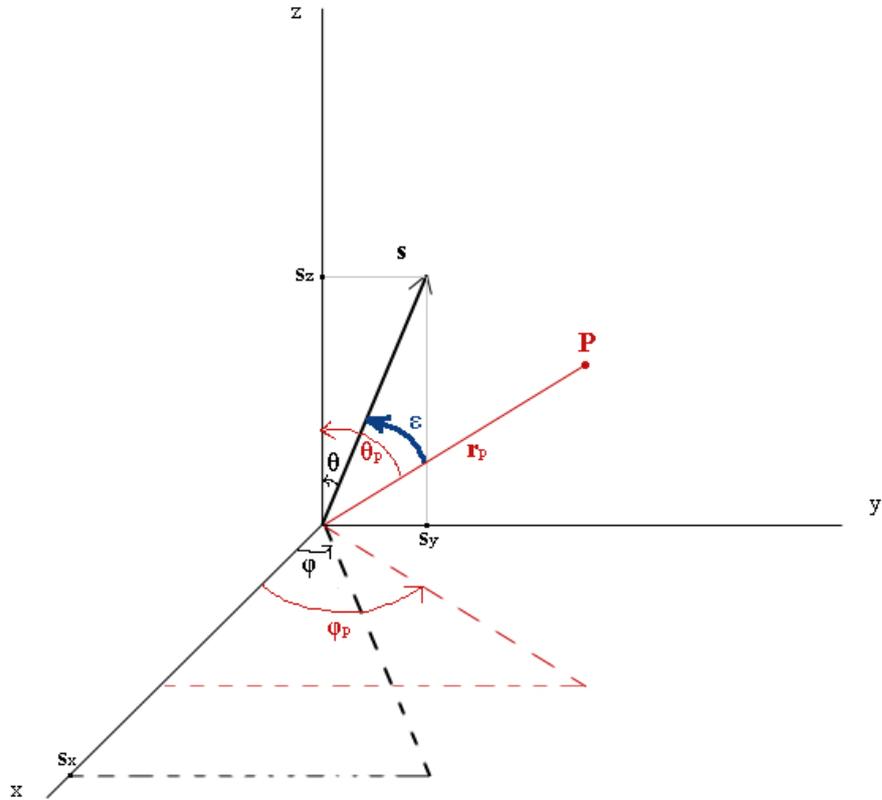
*Figure 2.2 **s** vector, any point P and ε, the angle between them*

Let the inclination and the azimuth angles for the vectors $\mathbf{g_0}$ and $\mathbf{g_1}$ be θ_0, φ_0 and θ_1, φ_1 respectively. From Figure 2.1;

$$\phi_0 = \phi_1 = \phi - \pi$$

$$\theta_0 = \frac{1}{2}\pi, \qquad \theta_1 = \frac{1}{2}\pi - \theta \qquad\qquad (2.1.13)$$

and then $\mathbf{g_0}$ and $\mathbf{g_1}$ now can be written as following;

$$\mathbf{g_0} = \sin\theta_0 \cos\phi_0 \mathbf{i} + \sin\theta_0 \sin\phi_0 \mathbf{j} + \cos\theta_0 \mathbf{k}$$

14

$$= \cos(\phi - \pi)\mathbf{i} + \sin(\phi - \pi)\mathbf{j}$$

$$= -\cos\phi\,\mathbf{i} - \sin\phi\,\mathbf{j} \tag{2.1.14}$$

$$\mathbf{g_1} = \sin\theta_1\cos\phi_1\mathbf{i} + \sin\theta_1\sin\phi_1\mathbf{j} + \cos\theta_1\mathbf{k}$$

$$= \sin(\tfrac{1}{2}\pi - \theta)\cos(\phi - \pi)\mathbf{i} + \sin(\tfrac{1}{2}\pi - \theta)\sin(\phi - \pi)\mathbf{j} + \cos(\tfrac{1}{2}\pi - \theta)\mathbf{k}$$

$$= -\cos\theta\cos\phi\,\mathbf{i} - \cos\theta\sin\phi\,\mathbf{j} + \sin\theta\,\mathbf{k} \tag{2.1.15}$$

To write **a** in spherical polar coordinates, equation (2.1.14) and (2.1.15) are used in the equation (2.1.9);

$$\mathbf{g_0} \cdot \mathbf{i} = -\cos\phi$$

$$(\mathbf{g_0} \cdot \mathbf{i})\mathbf{g_1} = \cos\theta\cos^2\phi\,\mathbf{i} + \cos\theta\sin\phi\cos\phi\,\mathbf{j} - \sin\theta\cos\phi\,\mathbf{k}$$

$$\mathbf{g_0} \cdot \mathbf{j} = -\sin\phi$$

$$\mathbf{g_1} \times \mathbf{s} = \begin{pmatrix} \mathbf{i} & \mathbf{j} & \mathbf{k} \\ -\cos\theta\cos\phi & -\cos\theta\sin\phi & \sin\theta \\ \sin\theta\cos\phi & \sin\theta\sin\phi & \cos\theta \end{pmatrix} = -\sin\phi\,\mathbf{i} + \cos\phi\,\mathbf{j}$$

$$(\mathbf{g_0} \cdot \mathbf{j})(\mathbf{g_1} \times \mathbf{s}) = \sin^2\phi\,\mathbf{i} - \sin\phi\cos\phi\,\mathbf{j}$$

$$\left[(\mathbf{g_0} \cdot \mathbf{i})\mathbf{g_1} + (\mathbf{g_0} \cdot \mathbf{j})(\mathbf{g_1} \times \mathbf{s})\right] =$$

$$\mathbf{i}\left[\sin^2\phi + \cos\theta\cos^2\phi\right] + \mathbf{j}\left[-\sin\phi\cos\phi + \cos\theta\sin\phi\cos\phi\right] + \mathbf{k}\left[-\sin\theta\cos\phi\right]$$

$$\mathbf{a} = fl_0\sqrt{\cos\theta}\left\{\mathbf{i}\left[\cos\theta + \sin^2\phi(1 - \cos\theta)\right] + \mathbf{j}\left[(1 - \cos\theta)\sin\phi\cos\phi\right] - \mathbf{k}\sin\phi\cos\phi\right\}$$

$$\boxed{\begin{aligned} a_x &= fl_0\sqrt{\cos\theta}\left[\cos\theta + \sin^2\phi(1 - \cos\theta)\right] \\ a_y &= fl_0\sqrt{\cos\theta}\left[(1 - \cos\theta)\sin\phi\cos\phi\right] \\ a_z &= -fl_0\sqrt{\cos\theta}\sin\phi\cos\phi \end{aligned}} \tag{2.1.16}$$

As a second step, **b** is written in spherical polar coordinates using (2.1.4);

$$\mathbf{b} = \mathbf{s} \times \mathbf{a} = \begin{pmatrix} \mathbf{i} & \mathbf{j} & \mathbf{k} \\ \sin\theta\cos\phi & \sin\theta\sin\phi & \cos\theta \\ a_x & a_y & a_z \end{pmatrix}$$

$$= fl_0\sqrt{\cos\theta}\left\{\mathbf{i}\left[\sin\phi\cos\phi(\cos\theta-1)\right] + \mathbf{j}\left[1-\sin^2\phi(1-\cos\theta)\right] - \mathbf{k}\sin\theta\sin\phi\right\}$$

$$\boxed{\begin{aligned} b_x &= fl_0\sqrt{\cos\theta}\sin\phi\cos\phi(\cos\theta-1) \\ b_y &= fl_0\sqrt{\cos\theta}\left[1-\sin^2\phi(1-\cos\theta)\right] \\ b_z &= -fl_0\sqrt{\cos\theta}\sin\theta\sin\phi \end{aligned}} \qquad (2.1.17)$$

After finding all components of both strength vectors, **a** and **b** in spherical polar coordinates, the final step is to find an expression for;

$$\frac{ds_x ds_y}{s_z},$$

which is indeed the usual infinitesimal solid angle, $d\Omega$. The expression for this is;

$$d\Omega = \sin\theta d\theta d\phi \qquad (2.1.18)$$

Substituting (2.1.18), (2.1.17), (2.1.16) and (2.1.11) into equations (2.1.2) and (2.1.3), components of the field vectors in spherical coordinates are found;

$$e_x = -\frac{iA}{\pi}\int_0^\alpha\int_0^{2\pi}\sqrt{\cos\theta}\sin\theta\left[\cos\theta+\sin^2\phi(1-\cos\theta)\right]\exp\left(ikr_P\cos\varepsilon\right)d\theta d\phi$$

$$e_y = \frac{iA}{\pi}\int_0^\alpha\int_0^{2\pi}\sqrt{\cos\theta}\sin\theta(1-\cos\theta)\sin\phi\cos\phi\exp\left(ikr_P\cos\varepsilon\right)d\theta d\phi \qquad (2.1.19)$$

$$e_z = \frac{iA}{\pi}\int_0^\alpha\int_0^{2\pi}\sqrt{\cos\theta}\sin^2\theta\cos\phi\exp\left(ikr_P\cos\varepsilon\right)d\theta d\phi$$

$$h_x = \frac{iA}{\pi} \int_0^\alpha \int_0^{2\pi} \sqrt{\cos\theta} \sin\theta (1-\cos\theta) \sin\phi \cos\phi \exp(ikr_P \cos\varepsilon) d\theta d\phi$$

$$h_y = -\frac{iA}{\pi} \int_0^\alpha \int_0^{2\pi} \sqrt{\cos\theta} \sin\theta \left[1-(1-\cos\theta)\sin^2\phi\right] \exp(ikr_P \cos\varepsilon) d\theta d\phi \qquad (2.1.20)$$

$$h_z = \frac{iA}{\pi} \int_0^\alpha \int_0^{2\pi} \sqrt{\cos\theta} \sin^2\theta \sin\phi \exp(ikr_P \cos\varepsilon) d\theta d\phi$$

Here $\cos\varepsilon$ is given by the equation (2.1.12), α is the angular semi-aperture on the image region, i.e., 2α is the angle which the diameter of the exit pupil subtends at the geometrical focus, and A is the constant;

$$A = \frac{kfl_0}{2} = \frac{\pi fl_0}{\lambda} \qquad (2.1.21)$$

The integration with respect to φ can be carried with the help of the following formulae which are valid for any integral value of;

$$\int_0^{2\pi} \cos n\phi \exp\left[i\rho \cos(\phi-\gamma)d\phi\right] = 2\pi i^n J_n(\rho) \cos n\gamma$$
$$\qquad (2.1.22)$$
$$\int_0^{2\pi} \sin n\phi \exp\left[i\rho \cos(\phi-\gamma)d\phi\right] = 2\pi i^n J_n(\rho) \sin n\gamma$$

where $J_n(\rho)$ is the *Bessel* function of the first kind and order n. Using the trigonometric identities; $\cos\varphi\sin\varphi = \frac{1}{2}\sin 2\varphi$ and $\sin^2\varphi = \frac{1}{2}(1-\cos 2\varphi)$, components of the field vectors at any point P in the image region can be written as the following;

$$e_x(P) = -iA(I_0 + I_2 \cos 2\phi_P)$$
$$e_y(P) = -iAI_2 \sin 2\phi_P \qquad (2.1.23)$$
$$e_z(P) = -2AI_1 \cos\phi_P$$

$$h_x(P) = -iAI_2 \sin 2\phi_P$$
$$h_y(P) = -iA(I_0 - I_2 \cos 2\phi_P) \qquad (2.1.24)$$
$$h_z(P) = -2AI_1 \sin\phi_P$$

17

where;

$$I_0 = I_0(kr_P, \theta, \alpha) = \int_0^\alpha \sqrt{\cos\theta} \sin\theta (1 + \cos\theta) J_0(kr_P \sin\theta \sin\theta_P) \exp(ikr_P \cos\theta \cos\theta_P) d\theta$$

$$I_1 = I_1(kr_P, \theta, \alpha) = \int_0^\alpha \sqrt{\cos\theta} \sin^2\theta J_1(kr_P \sin\theta \sin\theta_P) \exp(ikr_P \cos\theta \cos\theta_P) d\theta$$

$$I_2 = I_2(kr_P, \theta, \alpha) = \int_0^\alpha \sqrt{\cos\theta} \sin\theta (1 - \cos\theta) J_2(kr_P \sin\theta \sin\theta_P) \exp(ikr_P \cos\theta \cos\theta_P) d\theta$$

$$(2.1.25)$$

The results (2.1.23) and (2.1.24) represent the analytic solution of the problem [21] [23]. These express the electric and magnetic field at any point P in an aplanatic optical system with a point source, assumed to be at infinity, in the direction of the optical axis, in terms of three integrals I_0, I_1, and I_2.

2.2 Energy Density

2.2.1 Expression of the field vectors in optical coordinates

Diffraction systems with small angular aperture are mostly analyzed with certain "optical coordinates" for convenience [24] [25]. In the next section, energy density, which corresponds to the point spread function, for an optical system with small angular aperture is computed approximately, therefore it is convenient to introduce *new coordinates*, u and v at this stage [23].

$$u = kr_P \cos\theta_P \sin^2\alpha = kz \sin^2\alpha$$
$$v = kr_P \sin\theta_P \sin\alpha = k\sqrt{x^2 + y^2} \sin\alpha$$

$$(2.2.1)$$

From now on the subscript P shall be omitted in the azimuthal symbol φ_P and the three parameters of any point P are now, u, v, and φ; instead of spherical polar parameters r_P, θ_P, and φ_P. The geometrical focal plane is given by $u = 0$ and the axis by $v = 0$.
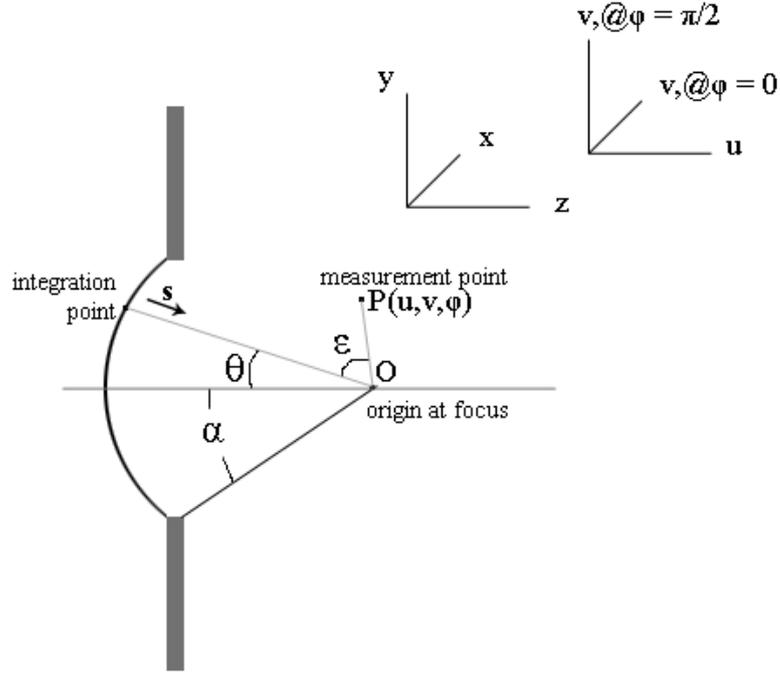
Figure 2.3 s vector, measurement and integration points, with a scheme of the Cartesian and the introduced coordinates

The three integrals (2.1.25) are now regarded as functions of u and v;

$$I_0(u,v) = \int_0^\alpha \sqrt{\cos\theta}\, \sin\theta(1+\cos\theta)J_0\left(\frac{v\sin\theta}{\sin\alpha}\right)\exp\left(\frac{iu\cos\theta}{\sin^2\alpha}\right)d\theta$$

$$I_1(u,v) = \int_0^\alpha \sqrt{\cos\theta}\, \sin^2\theta J_1\left(\frac{v\sin\theta}{\sin\alpha}\right)\exp\left(\frac{iu\cos\theta}{\sin^2\alpha}\right)d\theta \qquad (2.2.2)$$

$$I_2(u,v) = \int_0^\alpha \sqrt{\cos\theta}\, \sin\theta(1-\cos\theta)J_2\left(\frac{v\sin\theta}{\sin\alpha}\right)\exp\left(\frac{iu\cos\theta}{\sin^2\alpha}\right)d\theta$$

And the necessary angles are shown in Figure 2.3.

2.2.2 Energy Density of the System

The electric energy density, the magnetic energy density and the total energy density, each averaged over a time interval which is large compared to the basic period $T = \frac{2\pi}{\omega}$ are defined as the following [23] ;

$$
\begin{aligned}
\left\langle w_e(u,v,\phi)\right\rangle &= \frac{1}{8\pi}\left\langle \mathbf{E^2} \right\rangle = \frac{1}{16\pi}(\mathbf{e.e^*}) \\
\left\langle w_m(u,v,\phi)\right\rangle &= \frac{1}{8\pi}\left\langle \mathbf{H^2} \right\rangle = \frac{1}{16\pi}(\mathbf{h.h^*}) \\
\left\langle w(u,v,\phi)\right\rangle &= \left\langle w_e(u,v,\phi)\right\rangle + \left\langle w_m(u,v,\phi)\right\rangle = \frac{1}{16\pi}(\mathbf{e.e^* + h.h^*})
\end{aligned}
\tag{2.2.3}
$$

From (2.1.23), (2.1.24) and (2.2.3); energy densities can be written in terms of the integrals I_0, I_1, and I_2;

$$
\begin{aligned}
\left\langle w_e(u,v,\phi)\right\rangle &= \frac{A^2}{16\pi}\left\{ |I_0|^2 + 4|I_1|^2\cos^2\phi + |I_2|^2 + 2\cos\phi\, 2\Re(I_0 I_2{}^*) \right\} \\
\left\langle w_m(u,v,\phi)\right\rangle &= \frac{A^2}{16\pi}\left\{ |I_0|^2 + 4|I_1|^2\sin^2\phi + |I_2|^2 - 2\cos\phi\, 2\Re(I_0 I_2{}^*) \right\} \\
\left\langle w(u,v,\phi)\right\rangle &= \frac{A^2}{8\pi}\left\{ |I_0|^2 + 2|I_1|^2 + |I_2|^2 \right\}
\end{aligned}
\tag{2.2.4}
$$

where $\Re$ denotes the real part and the asterisk the complex conjugate.

Note that since $I_n(-u, v) = I_n{}^*(u, v)$ with, $n = 0,1,2$ in equations (2.2.2);

$$
\left\langle w_e(-u,v,\phi)\right\rangle = \left\langle w_e(u,v,\phi)\right\rangle_{,} \quad \left\langle w_m(-u,v,\phi)\right\rangle = \left\langle w_m(u,v,\phi)\right\rangle
$$

$$
\left\langle w(-u,v,\phi)\right\rangle = \left\langle w(u,v,\phi)\right\rangle
\tag{2.2.5}
$$

Therefore, the time averaged electric energy density distribution, the time averaged magnetic energy density distribution, and the time averaged total energy density distribution are symmetrical about the focal plane $u = 0$ [23].

Moreover, it is seen that;

$$\langle w_m(u,v,\phi)\rangle = \langle w_e(u,v,\phi - \tfrac{1}{2}\pi)\rangle \qquad (2.2.6)$$

Hence the distribution of the time averaged magnetic energy density is the same as the distribution of the time averaged electric energy density, except the distributions are rotated by 90˚ about the axis of the system, with respect to each other [23].

Final result from the analysis of the time averaged energy densities is based on the fact that $<w>$ is not a function of φ, i.e., the locations of constant time averaged total energy density are surfaces of revolution about the axis of revolution of the system [23].

2.3 Small Angular Aperture Approximation and the Point Spread Function

Paraxial approximation is used commonly in mathematical derivations in optics [26]. Despite this approximation does not seem suitable for many kinds of optical configurations, the differences between the real cases and the approximated predicts are not needed to be emphasized too much, since the general form of the function is unchanged [21] .

When the angular aperture of the system, α is small enough, and u and v and are not large compared to unity; the trigonometric factors in the amplitudes of the integrands in (2.2.2) can be replaced by the first term of their series expansion [23];

Making following replacements in equations (2.2.2);

$\cos\theta \rightarrow 1 - \theta^2/2$ in the exponentials,

$\cos\theta \rightarrow 1$ otherwise

$\sin\theta \rightarrow \theta$ and $\sin\alpha \rightarrow \alpha$

The integrals become;

$$I_0(u,v) = 2\exp\left(iu/\alpha^2\right)\int_0^\alpha \theta J_0\left(\frac{v\theta}{\alpha}\right)\exp\left(-iu\theta^2/2\alpha^2\right)d\theta$$

$$I_1(u,v) = \exp\left(iu/\alpha^2\right)\int_0^\alpha \theta^2 J_1\left(\frac{v\theta}{\alpha}\right)\exp\left(-iu\theta^2/2\alpha^2\right)d\theta \qquad (2.3.1)$$

$$I_2(u,v) = \tfrac{1}{2}\exp\left(iu/\alpha^2\right)\int_0^\alpha \theta^3 J_2\left(\frac{v\theta}{\alpha}\right)\exp\left(-iu\theta^2/2\alpha^2\right)d\theta$$

For small x, $J_n(x) \sim x^n$ and when this approximation is held, it is seen that I_1 and I_2 are of lower order in α than I_0. So, these integrals may be neglected in comparison with I_0. Therefore (2.1.23) and (2.1.24) reduce to;

$$e_x = h_y = -iAI_0 \qquad (2.3.2)$$

$$e_y = e_z = h_x = h_z = 0 \qquad (2.3.3)$$

Hence, in a small angular aperture system, the electric and magnetic fields in the image region are linearly polarized [23].

It is clearly seen that in the case of a small angular aperture, the image field might be defined just by one complex scalar, e_x or e_h, which depends only on the integral I_0.

The problem of interest has now become much simpler since only the thing to do is to evaluate the integral I_0 to get a compact form of the energy density which has now a form of;

$$\langle w_e \rangle = \langle w_m \rangle = \frac{1}{2}\langle w \rangle = \frac{A^2}{16\pi}\left|I_0\right|^2 \qquad (2.3.4)$$

To evaluate I_0, a new variable ρ is introduced; $\rho = \theta / \alpha$. Then, I_0 becomes [23];

$$I_0(u,v) = 2\alpha^2 \exp\left(iu/\alpha^2\right)\int_0^1 \rho J_0\left(v\rho\right)\exp\left(-\tfrac{1}{2}iu\rho^2\right)d\rho \qquad (2.3.5)$$

The integral above can be evaluated with the help of *Lommel* functions, U_n [27] [28].

$$U_n(u,v) = \sum_{s=0}^{\infty} (-1)^s \left(\frac{u}{v}\right)^{n+2s} J_{n+2s}(v)$$

$$\int_0^1 \rho J_0(v\rho) \exp\left(\tfrac{1}{2} iu\rho^2\right) d\rho = \frac{1}{u} \exp\left(-\tfrac{1}{2} iu\right) \left[U_1(u,v) + iU_2(u,v)\right]$$

(2.3.6)

Using (2.3.5);

$$I_0(u,v) = 2\alpha^2 \exp\left(iu/\alpha^2\right) \frac{1}{u} \exp\left(-\tfrac{1}{2} iu\right) \left[U_1(u,v) + iU_2(u,v)\right]$$

$$= \frac{2\alpha^2}{u} \exp\left[iu\left(\frac{1}{\alpha} - \frac{1}{2}\right)\right] \left[U_1(u,v) + iU_2(u,v)\right]$$

(2.3.7)

Substituting (2.3.7) into the equations in (2.3.2) and (2.3.3), it is found that;

$$e_x = h_y = -\frac{2iA\alpha^2}{u} \exp\left[iu\left(\frac{1}{\alpha} - \frac{1}{2}\right)\right] \left[U_1(u,v) + iU_2(u,v)\right]$$

(2.3.8)

$$\boxed{\langle w_e \rangle = \langle w_m \rangle = \frac{1}{2}\langle w \rangle = \frac{A^2\alpha^2}{4\pi} \frac{1}{u^2} \left\{\left[U_1(u,v)\right]^2 + \left[U_2(u,v)\right]^2\right\}}$$

(2.3.9)

Equation (2.3.9) is the *point spread function (PSF)* of an aplanatic optical system with a point source, assumed to be at infinity, in the direction of the optical axis.

The limit when u goes to zero can be computed to find the PSF in the focal plane [23].

$$\lim_{u\to 0} \frac{U_1(u,v)}{u} = \frac{J_1(v)}{v}, \qquad \lim_{u\to 0} \frac{U_2(u,v)}{u} = 0$$

(2.3.10)

Substituting (2.3.10) into (2.3.9), the point spread function in the focal plane is found as;

$$\langle w_e \rangle = \langle w_m \rangle = \frac{1}{2}\langle w \rangle = \frac{A^2\alpha^2}{16\pi} \left(\frac{2J_1(v)}{v}\right)^2$$

(2.3.11)

23

A compact form of the point spread function (equation (2.3.9)) gives a chance to get a plot of the point spread function in any appropriate software. In this study, MATLAB has chosen for this purpose due to its wide field usage. The details on how the graph of equation (2.3.9) was plotted are examined in Appendix.
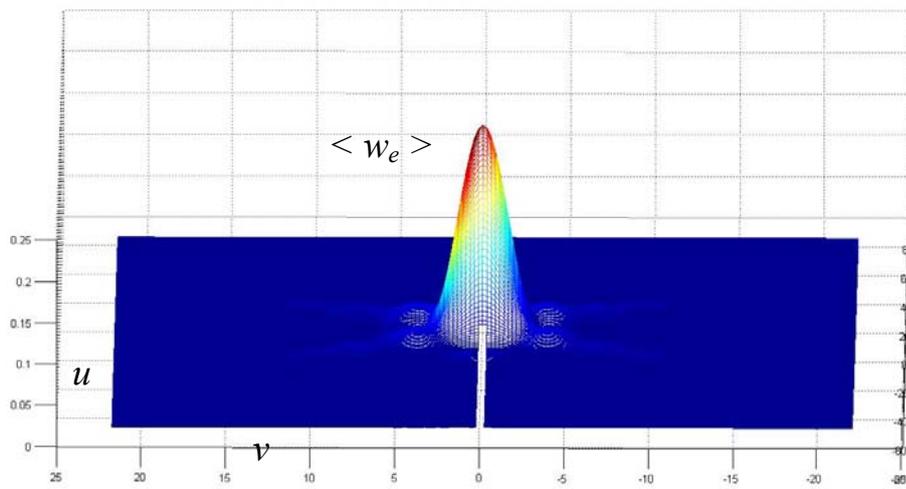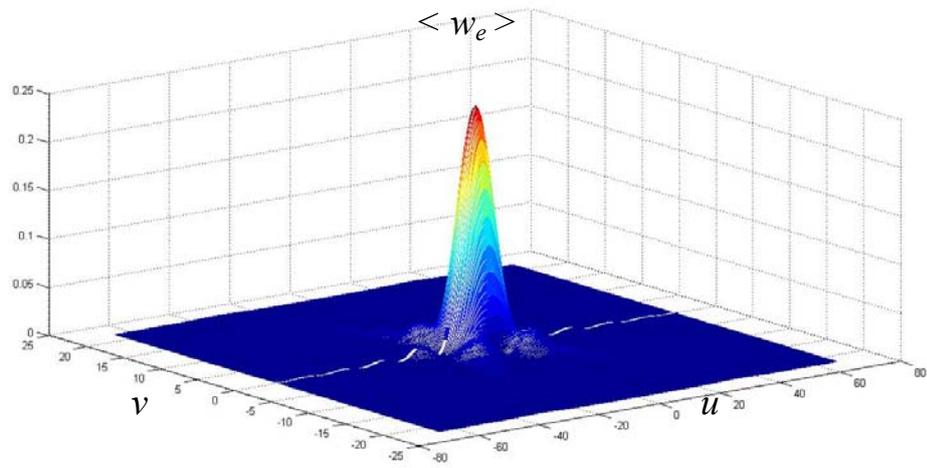
Figure 2.4 Graphs of the point spread function from two different point of views (equation (2.3.9))

2.4 Resolution

As it is mentioned at very beginning of the chapter, point spread function shows the intensity pattern illuminated by an optical system. The point spread function also defines the *resel*, the radius of the first dark fringe in the diffraction pattern, corresponds to the half of the biggest peak in $u = 0$ plane that is transverse to the optic axis [29] (Figure 2.5).
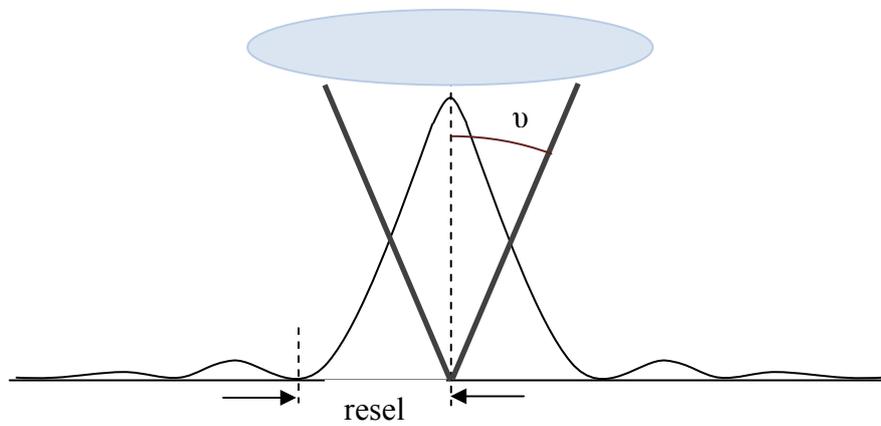
Figure 2.5 The resolution element, resel, due to a lens with a numerical aperture,

NA = nsinυ

So, one resel is the half size of the biggest peak of the transverse pattern in the focal plane, determined by equation (2.3.11). This size is the half of the Airy Disk's diameter[4], which is equal to [21] [30]:

---

[4] The definition of the Airy Disk is the pattern of the best focused spot of light that a perfect lens with a circular aperture can make, limited by the diffraction of light, named after George Biddell Airy(1801-1892).

$$d_{airy} = 1.22 \frac{\lambda}{NA} \qquad\qquad (2.4.1)$$

Then;

$$resel \equiv \Delta r = 1.22 \frac{\lambda}{2NA} = 1.22 \lambda f/\# \qquad\qquad (2.4.2)$$

One resel is the separation limit in order for being resolved of two observed points due to Rayleigh Criterion [21] [31]. There is 26% separation between two successive peaks [21] (Figure 2.6).
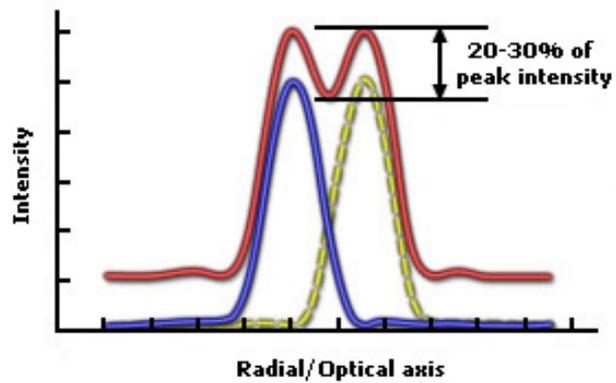
Figure 2.6 Rayleigh Limit, blue and yellow-dashed curves correspond to two "resolved" points

2.5 The Confocal Case

2.5.1 The Point Spread Function

The point spread function, the square of which gives the image of a confocal system has been examined in previous sections. In order to get a graph for the confocal case, it is necessary to add a line to redefine the function w as w^2 after the line 10 in the MATLAB code given in Appendix. The comparison of confocal and wide-field cases is given in Figure 2.7 with contour lines graphs.

a)

b)
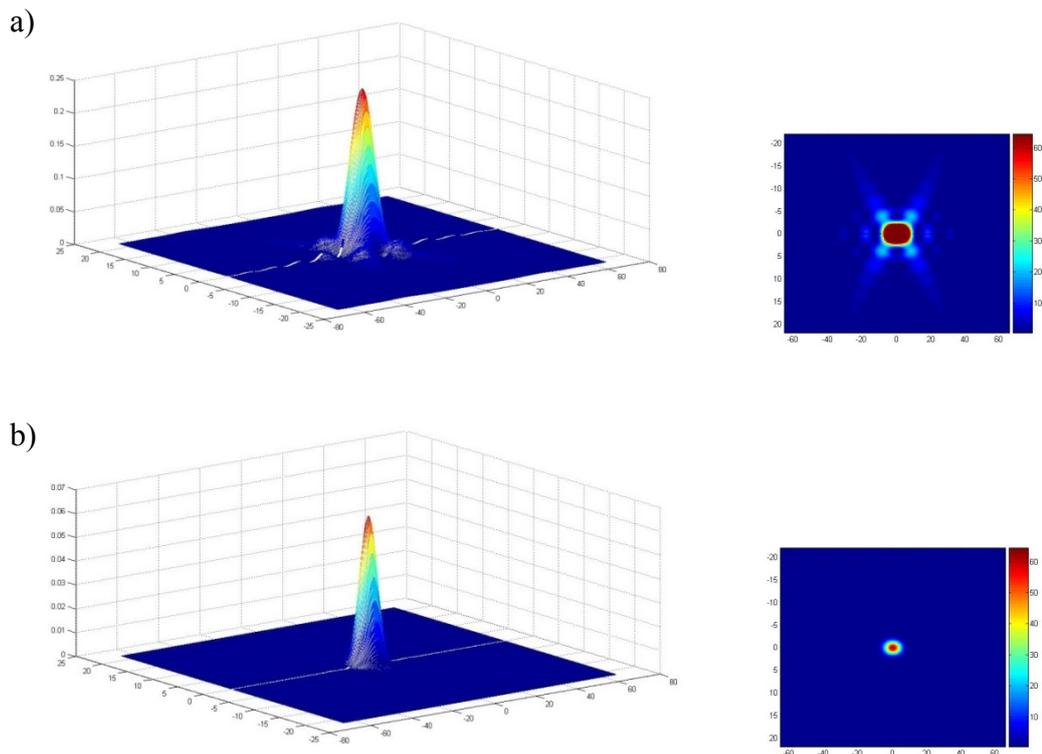
Figure 2.7 Comparison of point spread functions of a) the wide-field case and b) the confocal case

The intensity that corresponds to the major peak in the image of a confocal system is much greater than the peaks occurring around the focal point, as seen in Figure 2.7.b. This brings an advantage of having high contrast images contrary to the case of wide-field systems.

2.5.2 Lateral and Axial Resolutions

The comparison of the point spread functions in Figure 2.7 reveals that the confocal systems have sharper peaks than conventional systems. That also brings a change to the definition of the resolution. The common expression, derived empirically for the confocal radial resolution, in accordance with the Rayleigh Limit, is [21] [32];

$$\Delta r_{confocal} = 0.44 \frac{\lambda}{NA} = 0.88 \lambda \, f/\#$$ (2.5.1)

A confocal system provides a lateral resolution reduced by approximately 30 percent in comparison with conventional microscopes. It is also possible to resolve two points lying on the optical axis, i.e., to obtain 26% dip between two successive intensity maxima corresponds to an axial resolution with the definition of [21] [32];

$$\Delta z_{confocal} = 1.5 \frac{\lambda n}{NA^2} = 6 \lambda n \left(f/\# \right)^2$$ (2.5.2)

2.5.3 Gaussian Beam

In the focal plane $u = 0$, the point spread function has the mathematical form of;

$$p(0,v) = \frac{2J_2^2(v)}{v^2}$$ (2.5.3)

Along the optic axis $v = 0$, that is;

$$p(u,0) = \left(\frac{\sin(u/4)}{(u/4)} \right)^2 \qquad (2.5.4)$$

The concepts examined up to now are based on the assumption that the illumination overfills the pupil of the objective lens. That means a uniform irradiance. Laser illumination occurs in the form of Gaussian beams, and does not meet this condition. Laser beams have the intensity distribution of the form;

$$I(u,v) = I_0 \exp\left(-2v^2 / \omega(u) \right) \qquad (2.5.5)$$

Where u is the axial coordinate, v is the radial coordinate and ω is the parameter, often called "beam waist", described as the distance from the optical axis (beam radius) where intensity drops to $1/e$ of its maximum value [33].
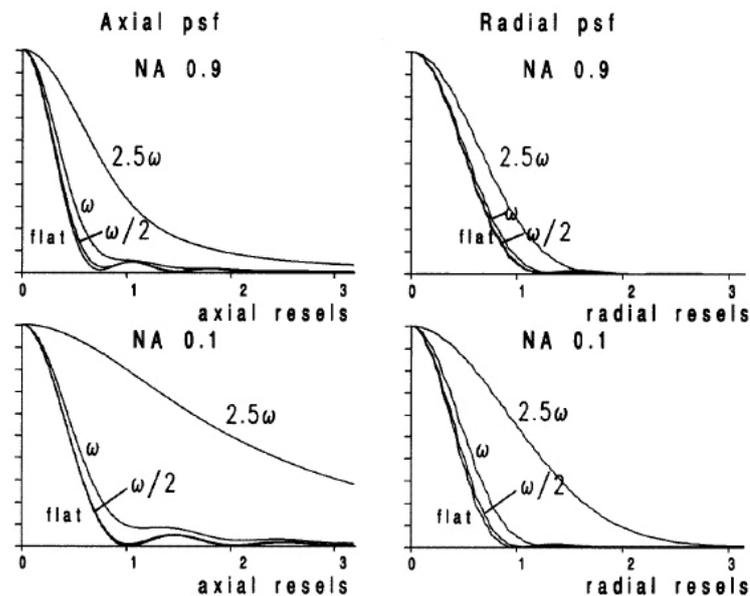
Figure 2.8 PSF's for two different lenses; one with NA=0.9, and the other one with NA=0.1, and for four ratios of Gaussian beam diameter to the pupil size (Adapted from [21])

30

If a beam with such an intensity distribution under-fills the pupil of the objective lens, it will be focused in the form of a Gaussian beam, eliminating the complexity of diffraction pattern. Gaussian patterns' drawback is that the resolution parameter –the minimum distance to resolve two different points- is large. If a beam partially fills the pupil, then the resulted pattern will be a mixture of the Gaussian and diffraction patterns [21] [34].

Webb's demonstration indicates intensity patterns for four ratios of the Gaussian beam diameter to the pupil size, for two different numerical apertures, 0.1 and 0.9 [21].

As shown in Figure 2.8, intensity distributions vary with the ratio of the Gaussian beam that fills the lens pupil. Over-filled pupils display a total diffraction pattern in accordance with formulae (2.5.3) and (2.5.4). Pupils cutting the Gaussian beam profile at 0.5ω and ω correspond to a pattern that is mixture of Gaussian and diffraction patterns. The ratio of 2.5ω is almost a total Gaussian pattern, resolution equals or is greater than 3 resels in all graphs.

Pupils cutting the Gaussian beam profile at 1ω seem the most reasonable choice since there is a little (14%) loss of light and the resolution is not affected much for this ratio.

2.7 Results and Discussion

Providing a theoretical background for confocal microscopy with the comparison of wide field microscopes was the aim of this chapter. In conclusion, since the PSF of a confocal microscope has sharper than the wide field one, it is possible to obtain high contrast images with confocal microscope. Furthermore confocal technique provides images with both lateral and axial resolutions 30 percent lower than the resolutions that can be obtained from a wide field microscope.

The intensity patterns of a uniformly illuminated (over-filled) and under-filled pupil by a Gaussian beam vary in both axes. Under-filled pupils result in low resolution,

31

yet, partially filled pupils result in a pattern of mixture of Gaussian and diffraction patterns, saving the major part of the light (in contrast with overfilled pupils), and compromising the resolution very little.

In the next chapter, the description of a home-built confocal microscope is given, which has been constructed in Middle East Technical University Terahertz Research Laboratory, in the light of the foregoing theoretical aspects.

CHAPTER 3

THE HOME-BUILT CONFOCAL MICROSCOPE

This chapter includes the description of a home-built confocal microscope designed in the Terahertz Research Laboratory in the Physics Department at Middle East Technical University. This microscope was designed to observe the practical results and verify the applicability of confocal technique in terms of resolution and contrast. Speed was not the first priority in this experiment, because DC servo motors were used to move the stages, and they were not very effective in scanning speed.

3.1 System Construction

Although the equipment used in the system was not ideal for well qualified imaging, it was sufficient to investigate metal surfaces based on confocal principles. The system was constructed by various optical components as well as the translation stages controlled by servo motors. The whole system is illustrated in Figure 3.1.

The source was 808 nm fiber-coupled diode laser. The reason for this choice is its compactness and size; i.e. it provides a power output of ~1 Watt. Besides, during the propagation of light through fiber, 808 nm light is less prone to intensity loss compared to other visible wavelengths.

As illustrated in Figure 3.1, the laser beam spreads as a point source. A 50:50 beam splitter mirror was placed in front of the fiber in order to transmit the reflected beam to the pinhole. The spread beam was focused by an objective onto the surface of the target metal object. Reflecting back from the metal surface, the laser beam was refocused by the objective onto the pinhole.
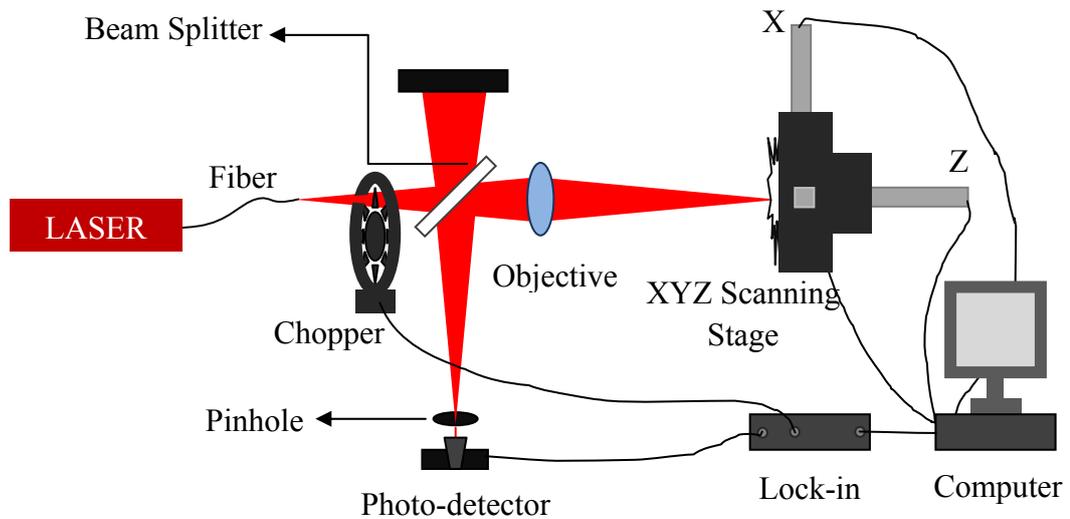
Figure 3.1 Home-Built Confocal Microscope

The word confocal stems from the configuration where the beam travels forward up to the sample in a path and back to the pinhole in another path that is conjugate to the first one. In other words, in the Home-Built Confocal Microscope illustrated above, the distance from the source to the objective lens is equal to the sum of the distances from the lens to the beam splitter, and from the beam splitter to the pinhole.

In confocal systems, it is the pinhole that provides the axial resolution [35]. The beam reflected back from the surface moving along the z axis is focused at various points after the objective, thus, in that way, the power of the light at those points vary in passing thorough the pinhole. The pinhole used in this system had a 100 μm diameter and it was placed in front of the photo-detector. That means only the part of the reflected beam, which was able to pass through a 100 μm diameter circular hole was collected by the detector, excluding the out of focus points.

Confocal laser systems typically use either photomultiplier tubes or avalanche photodiodes depending on the wavelength of the source, for their advantage of good

sensitivity and less noise [36] [37]. Since the detector to be used in this system was a regular Si-PIN photodiode, it was necessary to reduce the noise by doing phase sensitive detection of the returned signal by a lock-in amplifier (SR530 Dual Phase lock-in amplifier), and a mechanical chopping blade (SR 540, 5-spoke blade), rotating with 400 Hz frequency, connected to the lock-in, was placed just in front of the fiber exit for amplitude modulation.

The laser beam was first chopped for amplitude modulation, and then propagated across the beam splitter to the focusing objective. The objective with 2.5x magnification, focused the beam onto the metal surface, which was attached to the XYZ stage scanner, moving along all three directions. The stage scanner was driven by three separate servo motors, controlled by an algorithm written in the software Labview 7.1 during the time of study. The reflected beam passed through the objective and split up at the beam splitter mirror, focused onto the pinhole.

3.2 The Algorithm Controlling the System

To obtain the image of the metal surface, the surface had to be scanned by the laser beam and the voltage data on the lock-in amplifier had to be analyzed. An algorithm, for the purpose of both scanning the surface and take and transform the lock-in data to an electronic image was developed during the time of study. The scanning procedure is quite simple and illustrated in Figure 3.2.
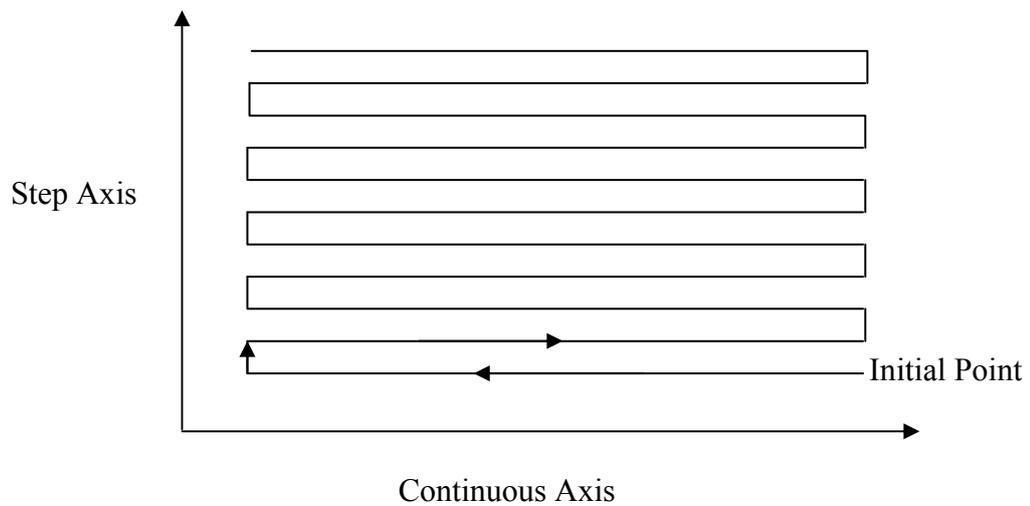
Figure 3.2 The scanning profile

As shown in Figure 3.2, one of the lateral axes is chosen as the continuous axis along which the stage is driven continuously starting from the initial point, whereas the other one, step axis, is moved in discreet steps. Arriving at the end of the distance determined for the continuous axis, it stops, and then, as soon as the step axis jumps to the next step it continues moving in the opposite direction. This procedure lasts until all the steps are scanned one by one.

Before initializing the scanning process, the initial and final positions of all axes, and other scanning parameters had to be determined. The interface of the program consists of two parts, XYZ control panels and scanning parameters. Both are shown in Figure 3.3.

The DC servo motors are open-loop, i.e. the positions of the axis are unknown to the computer in the first place. Therefore, the motors had to be initialized to a specific position before scanning. Once the absolute zero positions were defined for each individual motor, the stages were ready to start the scanning procedure.
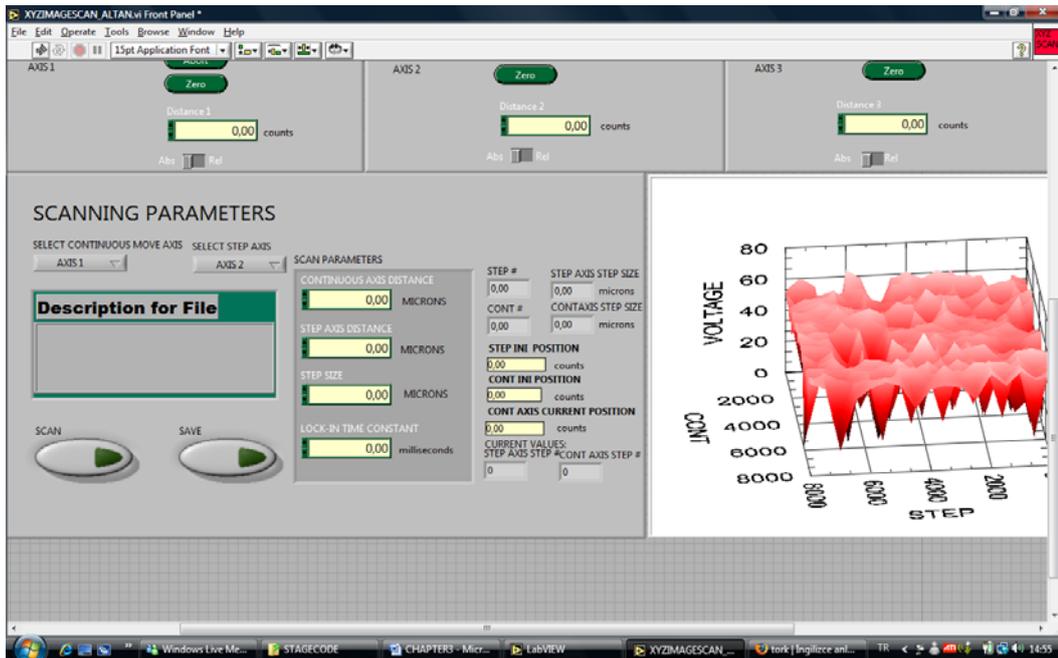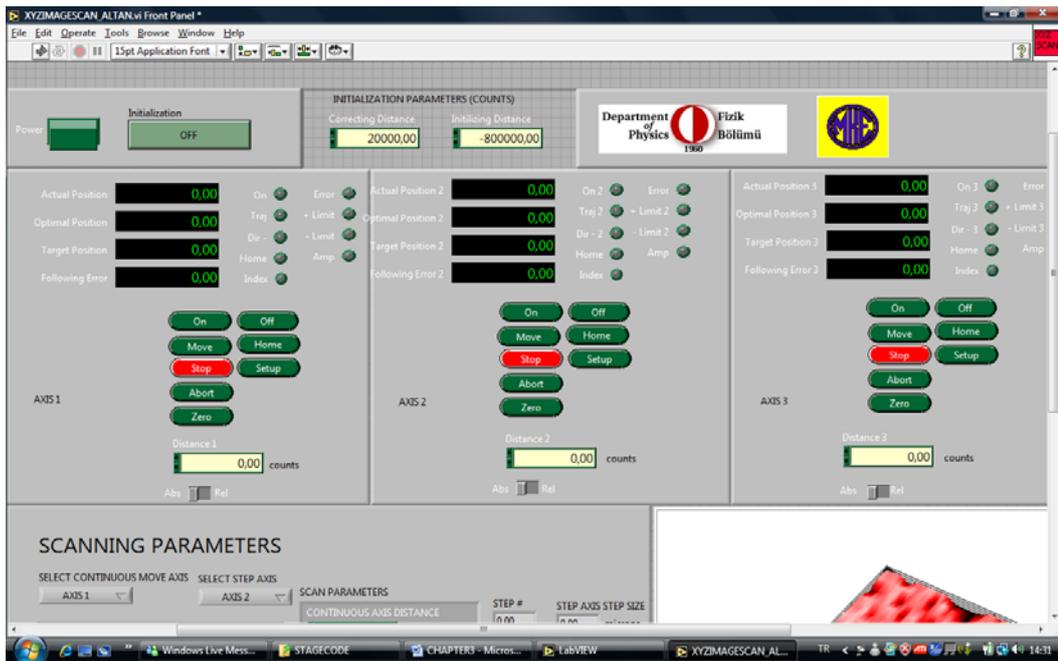
Figure 3.3 The interface of the program; control panels of the axes and the scanning parameters

3.3 Measurements

The laser source produces average output power in the order of 1 Watt. As the beam passes through the optical instruments, it loses a major part of its intensity until reaching the detector. At the objective the power was measured to be about 200mW and behind the pinhole, about10 mW. This amount was enough to obtain images of metal objects with at most 0. 3 mm defects on the surfaces.

A 1 Lira coin, exhibiting a Lambertian reflectance[5], was chosen as the object to be imaged. Figure 3.4 shows the two and three dimensional images of the metal surface obtained by the system.
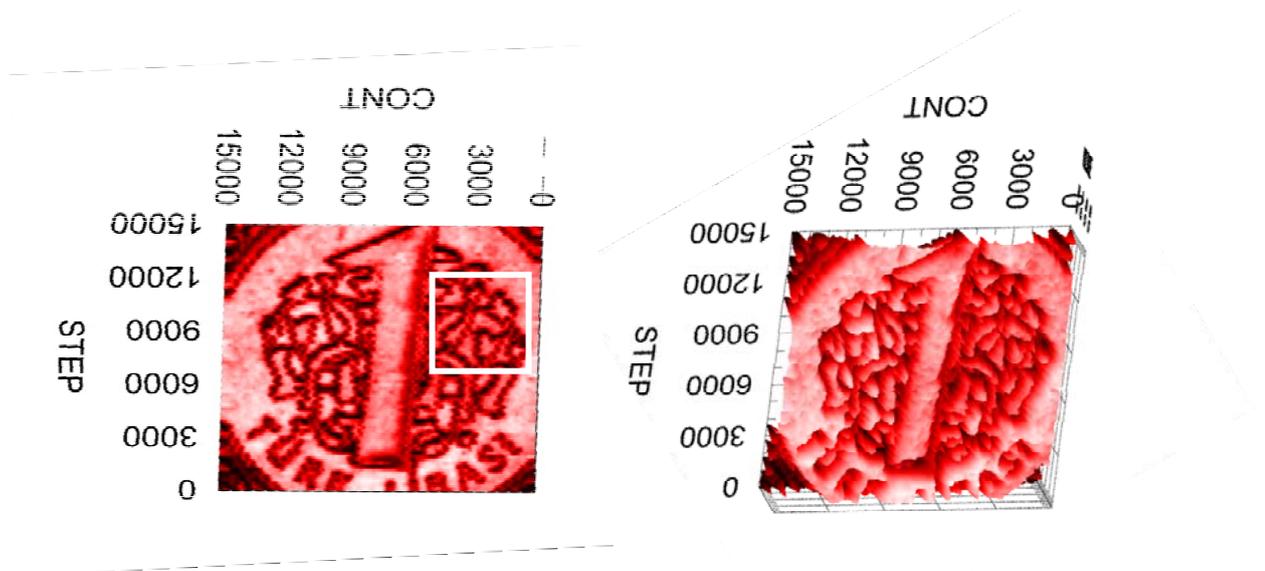
Figure 3.4 The image of a 15 mm x 15 mm area of the coin (right), and its three dimensional profile. The square area bordered white was scanned for a few times with different z positions.

---

[5] If a surface exhibits Lambertian reflectance, light falling on it is scattered such that the apparent brightness of the surface to an observer is the same regardless of the observer's angle of view.

The square area on the surface of the coin was scanned for 5 more times, at focal plane, at +1, -1, +5, and -5 mm away from the focal plane. These measurements were done to see the contrast variations at planes along z direction. As seen in figure 3.5, contrast differs as moving away from the focal plane in both directions. The images at +1 and -1 mm away from the focal plane display a decrease in contrast, and the images at +5 and -5 mm away from the focal plane contrast almost disappeared.

To see the effect of the size of the pinhole, a 20 micron pinhole was used instead of a 100 micron pinhole and the measurements were repeated. Figure 3.6 show three images taken at the focal plane, +1 and -1 mm away from the focal plane.
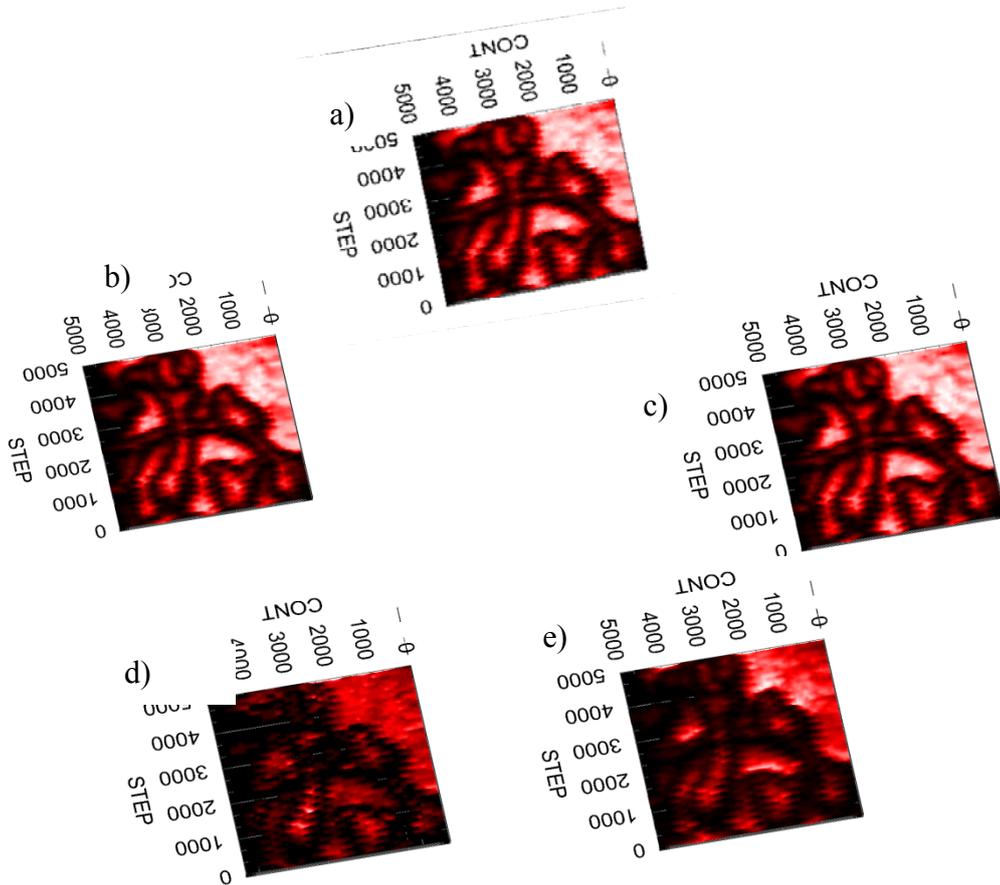
Figure 3.5 Images of a 5 mm x 5 mm area of the 1 Lira coin taken at a) the focal plane b) +1mm c)-1mm d)+5mm e)-5mm away from the focal plane

Reduction of the size of the pinhole resulted in decrease in contrast with even small distances away from the focal plane, as expected.

In Figure 3.6, in the image taken at the plane the dark (low) and the bright (high) areas appears more distinctive compared to the other images. In the images taken at +1 and -1 mm away from the focal plane, the dark areas seem to be brightened and the bright areas get dark. That emphasizes the significance of the confocal technique which provides high contrast and resolution in z direction.
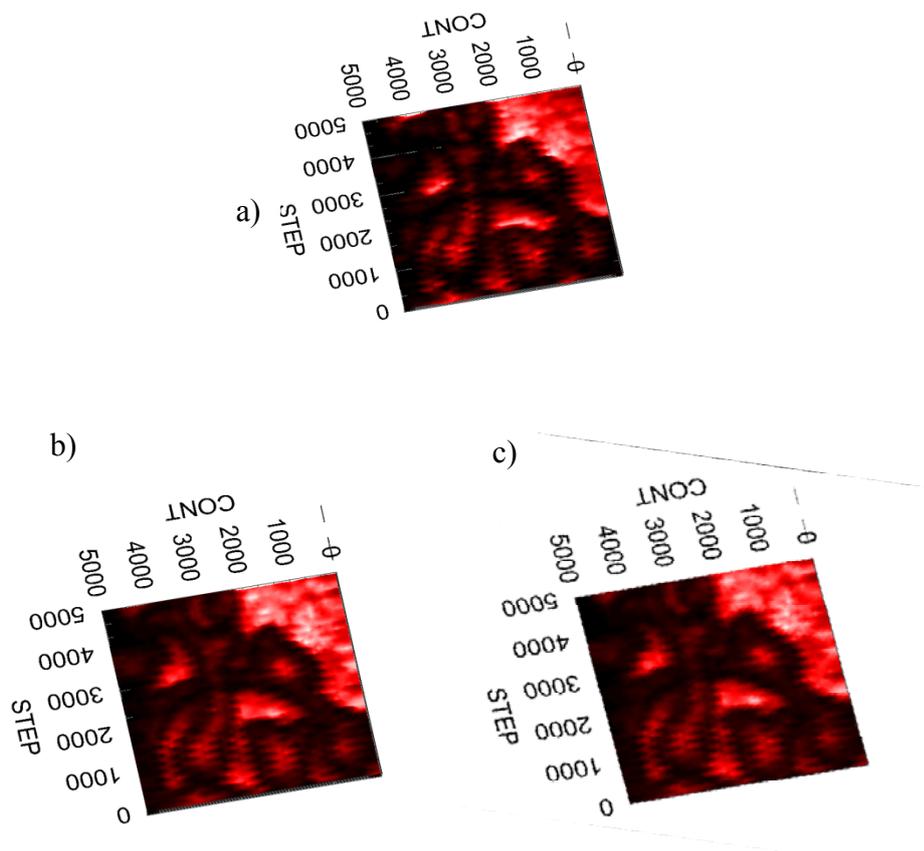
Figure 3.6 Images of a 5 mm x 5 mm area of the 1 Lira coin taken by a 20 micron pinhole at a) the focal plane b)+1mm c)-1mm away from the focal plane

3.4 Results and Discussion

The home-built microscope described in previous sections was designed for the purpose of examining the practical results of the confocal principles in terms of resolution and contrast.

Measurements indicated that it was possible to obtain both two and three dimensional views of metal surfaces by a system based on confocal technique. The theoretical resolution values might be calculated by the equations (2.5.1) and (2.5.2).

$$\Delta r_{confocal} = 0.44 \frac{\lambda}{NA} = 5.08 \mu m$$

(3.4.1)

$$\Delta z_{confocal} = 1.5 \frac{\lambda n}{NA^2} = 371.02 \mu m$$

The wavelength, λ, of the laser was 808 nm, the refractive index, n, of the objective was 1.5, and the numerical aperture, NA, of the objective was 0.07. The resolution values calculated above were the ideal results for these specific optical parameters. If the optical instruments were revised for better resolution values, it would be possible to lower them. The limitations to obtain those resolution values might be counted as the step size of the scanning process and the choice of size for the pinhole.

The step axis was driven with a step size of the order of 100 μm in almost all measurements. Therefore it was impossible to reduce the lateral resolution above this value. The smaller the size of the steps, the longer the time of the scanning processes. The servo motors travel a distance of 25 mm in 67 seconds, which means the scanning speed was 0.31×10^{-3} m/s. For instance, scanning of a 25 mm x 25 mm area would last about 2 days if the step size was arranged as 10 microns. Such a scanning may last a time of the order of minutes by strong motors, one of which was used for the systems described in next chapter.

The pinhole has a great significance in confocal systems, since the optical instrument that makes possible to resolve two separate points on a plane longitudinal to the optical axis is the pinhole. The larger the pinhole, the more photons pass through it, but, also the less selection of focal volume among scattered light, i.e., the more

41

photons reflected back from the out of focus points are collected. The pinhole has nothing to do with the PSF of the image; in fact it describes area in the object plane from which the photons are collected. PSF is related with the numerical aperture of the objective lens [21]. Still, the choice of the optimum pinhole size has to be determined by the resolution parameter, and thus the PSF. A pinhole smaller than one resel does not improve resolution, it just loses light. A pinhole that is equal to one resel allows full use of the objective lens' resolution, but does not actually change the resolution. A pinhole three resels across seems to be a good compromise [21] [38];

$$D_{opt} = 3M\Delta r_{confocal} = 3M\frac{0.44\lambda}{NA}$$ (3.4.2)

where λ is the wavelength of the source, M and NA is the magnification and the numerical aperture of the objective lens. The optimum pinhole diameter for the home-built confocal microscope is therefore;

$$D_{opt} = 38.1\mu m$$ (3.4.3)

The pinholes used in measurements of the home-built confocal microscope have the diameter sizes of 100 and 20 microns. Both pinhole sizes were comparable with the calculated value. The 20 micron diameter pinhole was able to collect less intense light the images were dim compared to ones obtained by the 100 micron diameter pinhole. However, the 20 micron diameter pinhole displays a decrease in contrast with even small distances away from the focal plane as emphasized in the comparison of the Figures 3.5 and 3.6.

In the next chapter, the developments of two systems based on two different wavelengths, one at 808 nm and one at 1550 nm, will be discussed. Both systems are fiber optic systems which, except the light being guided inside a fiber, are very similar to free-space systems.

CHAPTER 4

A FIBER OPTIC CONFOCAL MICROSCOPE

In this chapter the systems to be described are fiber-based systems. Fiber optical systems are very similar to free space systems; the only difference is that the light is guided in a fiber usually for the advantage of carrying the light in any desired path safely. Since the final aim is to design an imaging system for the measurements of the surfaces of rifled gun barrels, i.e. the surfaces to be imaged are not flat but cylindrical and the surface to be imaged is well inside a barrel whose length can be from about 10 cm to over 70 cm, so that the optical design of the system would be much easier with fibers.

4.1 Gun Barrels

In this project our goal was to analyze the inner surfaces of three different kinds of gun barrels, namely gun barrels used in the G3, H&K33 and MP5 automatic rifles. The G3 gun barrel has a length of 450 mm and a bore diameter of 7.62 mm. The H&K33 gun barrel has a length of 500 mm and a bore diameter of 5.56 mm. And finally the MP5 gun barrel has a length of 200 mm and a bore diameter of 9 mm. An example of a rifled bore is shown below. Figure 4.1 shows the picture of a sample 5.56 mm rifled gun barrel and a cross-section view of a barrel pointing the groove and the bore diameter.

As it is seen in the below diagram the diameter of the gun barrel is not constant but changes from a maximum inner diameter that can be up to 20 mm to a minimum diameter given by the bore diameter as was mentioned before.
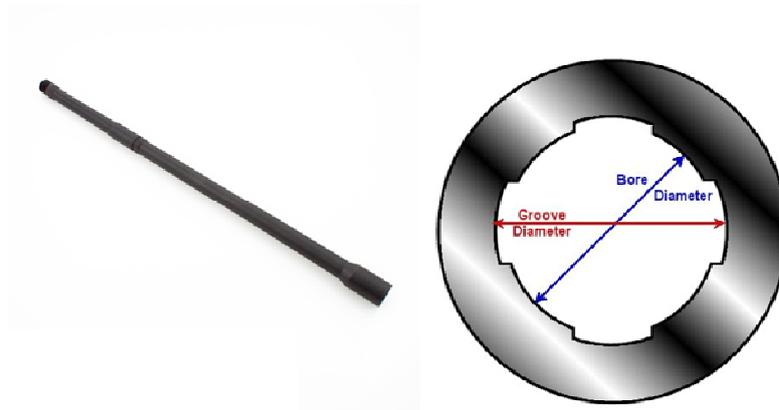
Figure 4.1 5.56 mm sample barrel (left), illustration of the cross-section of a 4-grooved barrel (right)

In addition to the changing inner diameter the inside of the gun barrel is rifled, and these grooves can have a depth of 0.1 mm. These groves allow for the projectile to travel in a straight path with a greater velocity. Since these grooves affect the motion of the projectile it is also important to measure the depth of the groove and if there are any scratches of deep cuts along the gun barrel. The initial analysis of the three rifled gun barrels, with inner diameters of 5.56 mm, 7.62 mm, and 9.00 mm showed that;

- the bore diameter may be extended to 12 mm at one end
- the groove diameter and the bore diameter are not equal to each other
- the depth size of the grooves are at least 0.1 mm

The goal is to measure the diameter at points along the gun barrel and whether there are any scratches or burrs or other deformations that can hinder the motion of the projectile inside the gun barrel. In order to perform these measurements the use of two different optical systems were explored using fiber optics, wide-field imaging system and a confocal imaging system.

44

Both systems will be used for measurement of rifled gun barrels and the aim is to measure the defect size at a precision of 0.01 mm on the surfaces of these barrels. The fiber optical system was designed to be incorporated into a mechanical system which could deal with rifled gun barrels of a maximum length of 1 m and inner diameter between 5.5-20 mm.

4.2 Mechanical Design

The system works basically as the rifled barrel moves back and forth on a linear slide and at the same time rotates around its translational axis inside a rotational slide, while the stationary imaging system, placed inside a tube inside the rifled barrel, scans the surface of the barrel.

Figure 4.2 Optical board (left), mechanical support frame (right); slides and the laser system were placed on this platform.

The slides and the optics were placed onto a platform constructed by two components, a breadboard and a support frame, shown in Figure 4.2.

Both the board and the support frame have 1500 x 900 mm size, the height of the board is 25 mm and the height of the support frame is 800 mm.

The pictures of the linear and the rotational translation stages are shown in Figure 4.3. There is a 50 mm diameter hole in the middle of the rotational translational stage. An additional component was necessary to attach the barrels with diameters 5.5-20 mm. This component, a three-prong clamp with a hole in the middle, also shown in Figure 4.3, was attached to the rotational axis to hold the barrel steady, and the rotational axis was attached to the linear axis to provide both translational and rotational motion at the same time.

Figure 4.3 Rotational translational stage (above, left), the component to be placed on the rotational axis (above, right), rotational translational stage attached to the linear translational stage (below)

The system construction was completed and the test measurements were done by using metal cylindrical rods of similar weights with the barrels. The rotational speed

of the system was 600 cycles/min, and even though the mirror axis was properly attached to the rotational translational stage axis, there were microscopic spaces between the axis of the rod and the axis of the mirror, resulting in vibrations. In fact, these vibrations were visible at the end of the rod, away from the mirror. So the design of the system had to be revised in order to avoid these vibrations affecting the imaging process.

The development studies were completed with a final design shown in Figure 4.4. The additional components were inserted to the system to provide a proper rotational movement without vibrations. It is also considered that the extra components should not cause a torque effect due to their weights; therefore Rexroth-Bosch type aluminum profiles, light and not flexible, were preferred [39]. A tack weld translational stage was placed to the system to hold the back end of the rod as well in order to reduce vibrations. The tack weld translational stage is shown in Figure 4.5.
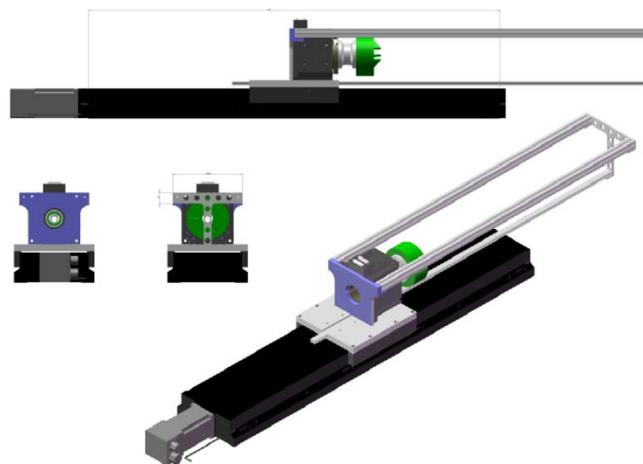
Figure 4.4 Various views of the final design of the translational stage system

There is an 8 mm diameter hole inside the tack weld, allowing the tube, which has a diameter of maximum 5 mm, covering the optical imaging system inside, to be placed through it.

Another concern was the tube covering the imaging system. Since the barrels to be measured could range from 5.4 mm to 20 mm in diameter and up to 1 m in length, a tube in accordance with these sizes had to be integrated into the system. One of the most vital issues was the inner diameter of the tube, because the outer diameter had to be at most 5.4 mm and the wall-thickness of the tube to be at least 1-2 mm for a rigid form.
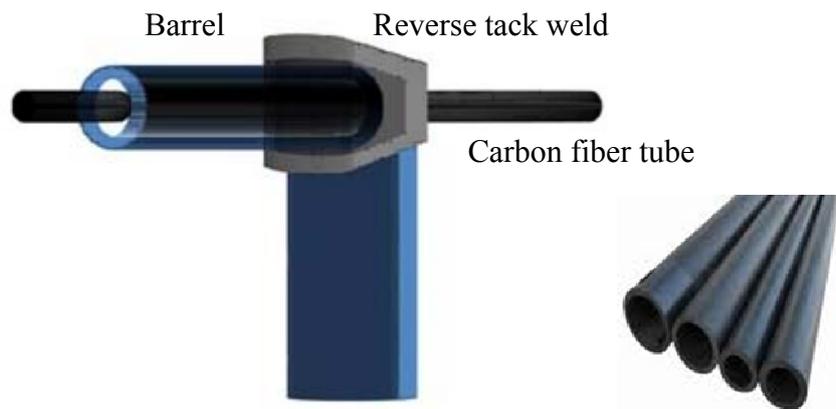
Figure 4.5 The tack weld translational stage (left), carbon fiber tube (right)

In addition, the inner diameter of the tube where the fiber bundles and other optical instruments were to be placed had to be as large as possible to simplify the construction. A rigid tube such as a tube made out of stainless steel was not available commercially for these required diameters and wall thicknesses. Since this was not a

realistic option, the best choice would be a material, as tough as stainless steel, temperature compensated, and not flexible; carbon fiber. (Figure 4.5) A carbon fiber tube with 5.3 mm outer diameter and 3.4 mm inner diameter was chosen as the host for the optical imaging system. Mechanical measurements that were performed on the tube in the gun barrel system, verified that there were no bending or loss of rigidity.
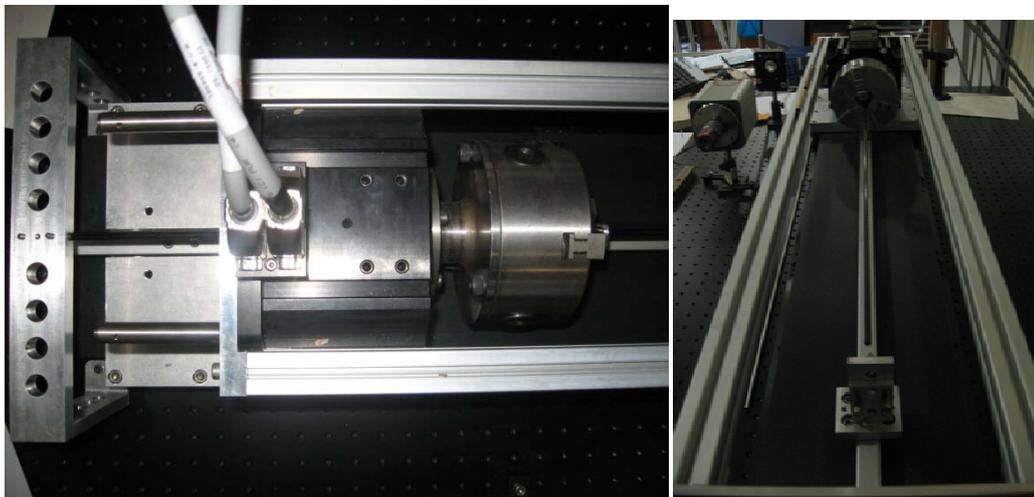
Figure 4.6 Pictures viewing the system from above (left), and frontally (right)

The pictures of the system viewing the mechanical component holding the fiber carbon tube and the tube integrated to the whole translational stage system are shown in Figure 4.6.

After all mechanical components were selected and constructed for the imaging system, user safety was considered. During the imaging process, the barrel will be rotated around the axis between the tack weld and the three-prong clamp and at the

same time it will be translated back and forth on the linear translational stage. After reviewing systems of similar construction it was concluded that the whole motion should take place inside a safety cage, and the control and power cables connected to the rotational translational stage will be in a cable tray, as shown in Figure 4.7.
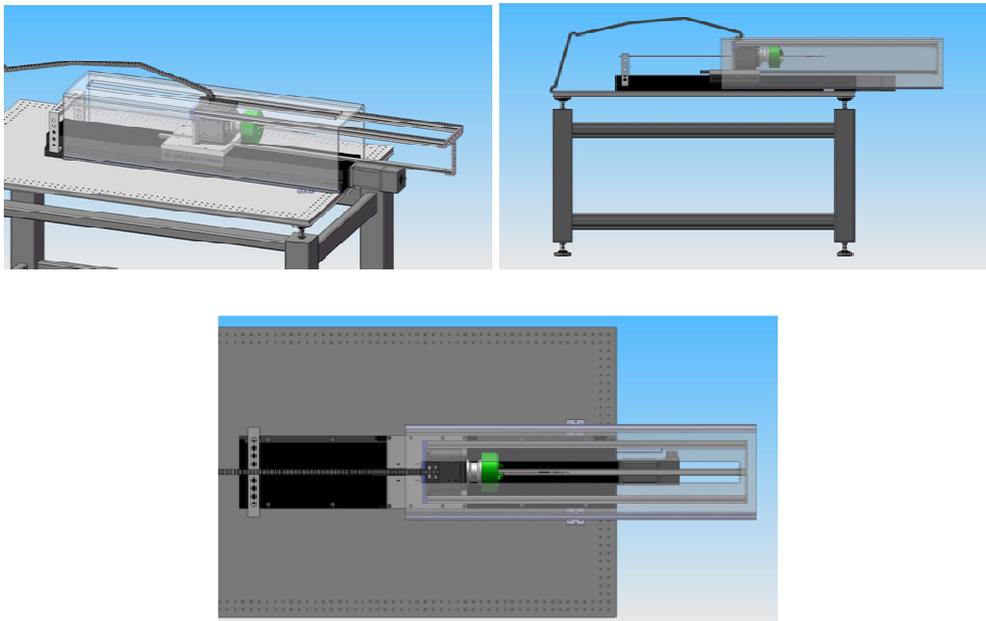
Figure 4.7 The safety cage and the cable tray around the translational stage system

4.3 Optical Design

As it was mentioned at the end of Chapter 3, two different optical systems with two different wavelengths were designed; one optical system was based on the wide field imaging technique, while the other one was based on the confocal technique.

The optical systems had to be placed inside a carbon fiber tube having 3.4 mm inner diameter. Since this size is not very large, the optics to be used in the systems had to be compatible with this requirement. Optical circulators, widely used in advanced communication systems and fiber optic sensor applications, would provide convenience by allowing the use of only a single fiber instead of two to make light propagate in both the forward and back directions. An optical circulator is a special fiber-optic component that can be used to separate optical signals that travel in opposite directions in an optical fiber. It is a three-port device designed such that light entering any port exits from the next. This means that if light enters port 1 it is emitted from port 2, but if some of the emitted light is reflected back to the circulator, it does not come out of port 1, but instead exits from port 3. A basic scheme of an optical circulator is illustrated in Figure 4.8.
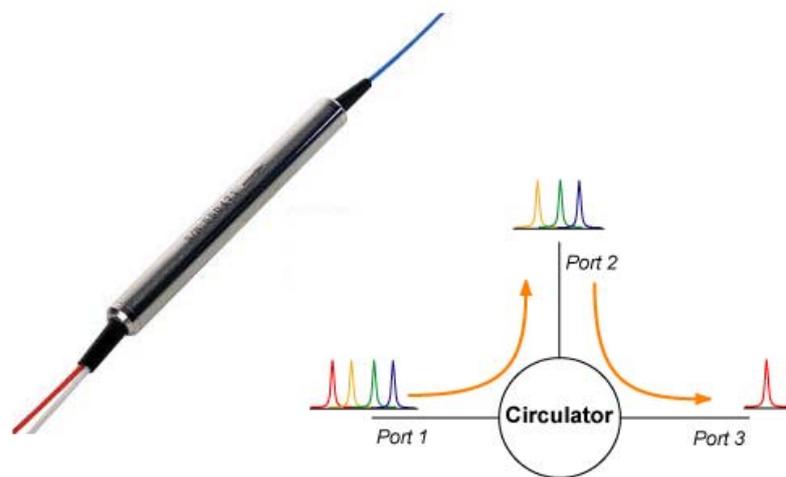
Figure 4.8 An optical circulator simplified diagram that shows its working principle: A multi-colored input is sent into port 1, the colors go to port 2, at port 2 there is a reflective surface which only reflects the red component. The red component is detected in port 3. (Adapted from www.thorlabs.de)

51

Apart from the size, the optical system had to be compatible with the measurements of various sized inner diameter gun barrels from about 5.5 mm to 20 mm. To make the lens focus the beam onto the surface of these different inner diameters, a movable small right angle prism (l x h: 2 mm x 2 mm) with a metallic polish was integrated into the system. A simple illustration of the optical design is shown in Figure 4.9. In Figure 4.10, an illustration and a photograph of the optical system integrated into the carbon fiber bore are shown.
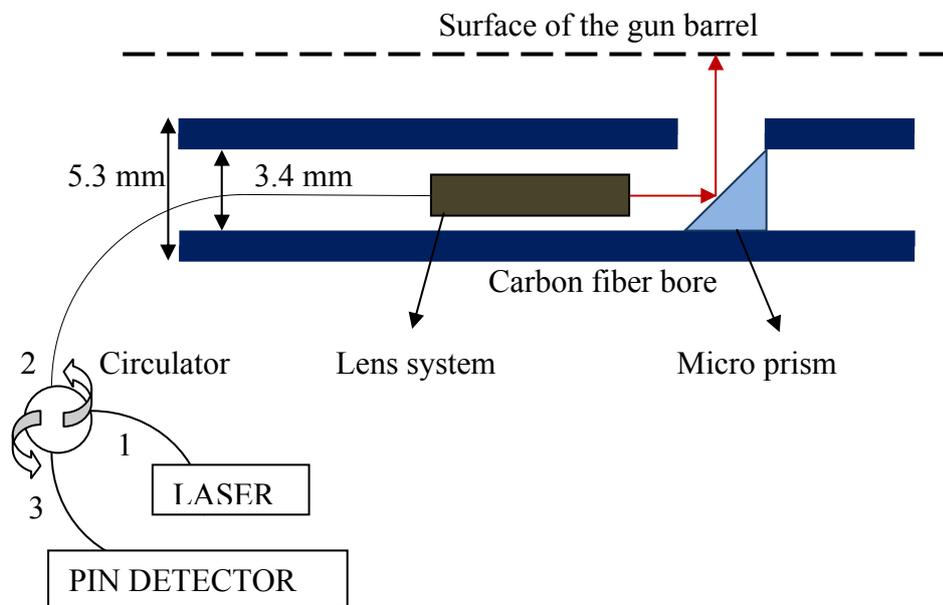
Figure 4.9 The schematic of the optical design

The illustration shown above is valid for both confocal and wide field systems. The component called "lens system" in Figure 4.9, corresponds to the wide field imaging optics and the confocal imaging optics. The main difference of these two systems

was based on the diameters of the fiber cores; in fact, this core serves as the pinhole that collects the reflected beam back from the surface of the gun barrels [40].
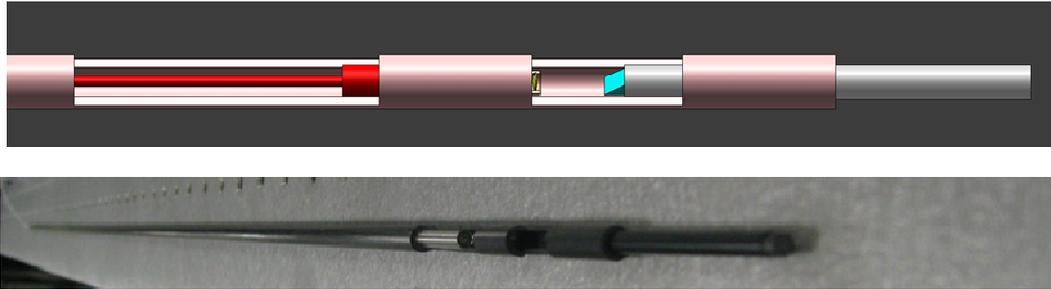
Figure 4.10 An illustration (above) and a photograph (below) of the optical system integrated into the carbon fiber bore

4.3.1 Wide Field Imaging System

In the wide field system, a 1550 nm diode laser source was used (Anritsu 1mW Laser Source with FC output). This laser diode was connected to port 1 of a connectorized optical circulator with single-mode fibers that worked at this wavelength. Port 3 of this circulator was connectorized and connected to a fast InGaAs photodiode (Thorlabs PDA50) with FC input. Port 2 of the circulator was connectorized to a pigtailed GRIN lens fiber collimator (Thorlabs 50-1550-FC). This fiber collimator was placed in a Teflon housing where an aspheric AR coated lens with 5 mm focal length and 2 mm diameter (Edmund Optics) was placed in front of it and was used to focus the beam onto the surface of the metal object. The diameter of the exit pupil of the collimator was 1.8 mm, and the beam diameter at the fiber exit was 0.5 mm. The diameter of the outer shell of the collimator lens/fiber housing was 3.4mm, a perfect

fit into our carbon-fiber tube. However, since initial measurements were performed on reflective metal surfaces and not gun barrels, the collimator was not placed inside the carbon fiber tube. The illustration of the wide field imaging system design is shown in Figure 4.11.

In the wide-field system the source was coming out of a single-mode fiber so, the mode profile was TEM_{00} mostly, resulting in the smallest spot size among other modes.
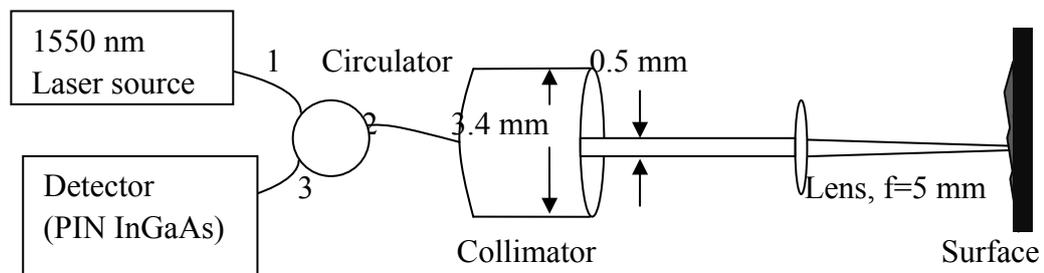
Figure 4.11 Illustration of the wide field imaging system design

4.3.2 Confocal Imaging System

In the confocal system, the source that was used was a 808 nm diode laser (Crystal Lasers, 1W Diode Laser with FC output optimized for 200 micron large core diameter fibers). After much investigation an optical circulator that was designed for a working wavelength of 850 nm is chosen (Optolink, OLCIR-M-3-085-500-25-NC 50/125 Multimode Optical Circulator). It was difficult to find a commercial optical circulator compatible with a 808 nm wavelength laser source. Since a wavelength of 850 nm is used in telecommunication systems it was decided to

54

choose a circulator that has a wide band transmission at this wavelength. In addition, since the laser power was near 1W, a MM-fiber circulator that can handle larger power due to its larger core size was chosen. The ports of this circulator were configured in the same manner as mentioned above, however port 3 was configured to a FC coupled APD-Si detector (Thorlabs/Menlo Systems APD-Si photodiode). And the output, port 2, was configured so that a special 25 micron core diameter fiber with a focusing lens at the end could be used. The focusing lens system at the end of the special fiber which had a 25 micron fiber exit pupil had an aspheric AR coated lens with a diameter of 2.5 mm. The 25 micron core of the fiber can also be understood as a 25 micron diameter pinhole that will collect the reflected beam back from the surface of the gun barrel and then transmit it to the photo detector.

In both wide-field and confocal systems, aspheric lenses were chosen because of their surface profile that reduces or eliminates spherical aberrations and other optical aberrations, contrary to a simple spherical lens.
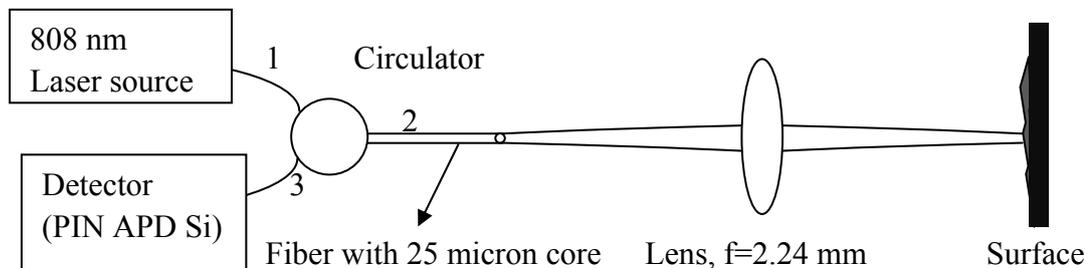
Figure 4.12 Illustration of the confocal imaging system design

The illustration of the confocal imaging system design is shown in Figure 4.12. The focal length of the lens was 2.24 mm and the detector was a Silicon avalanche photodiode.

4.4 Measurements and Calculations

A first measurement was performed by using the wide field imaging system with 1550 nm diode laser source. The distance from the GRIN lens/fiber collimated exit to the objective lens and the distance from the objective lens to the metal surface were both 5 mm. The focal length of the lens was 5 mm and the diameter of the lens was 2 mm, corresponding to a lens with a numerical aperture of 0.2. The spot size of the beam on the surface of the metal can be calculated by the formula below [41] [42];

$$\omega = \frac{f\lambda}{\pi\omega_0}$$
(4.4.1)

where f is the focal length of the lens, 5 mm; λ is the wavelength of the source, 1550 nm; ω_0 is the minimum beam radius, i.e., beam radius at the fiber exit, 250 μm; and ω is the beam radius at the focal point. The spot size diameter is calculated as 19.7 μm. This value is the minimum spot size that can be obtained from such a system. Using Rayleigh criterion: that the minimum distance between two observable points is given by the dip in intensity of those two points of 26%, the minimum radial resolution is calculated to be 2 x 3.85 μm = 7.70 μm. Since the system construction was based on wide field imaging technique, axial resolution cannot be assessed.

To test the image quality at this wavelength, a scanning system similar to the one discussed in chapter 3 was built. The motorized XYZ stage that was used could scan 25mm x 25mm in the vertical plane. A metal disk with the letter "A" scratched on the surface was placed in front of the focused beam. The metal disk was positioned so that it was nearly 5mm to the front of the lens. Since the stage moved very slowly we took large step sizes in the x and y directions. The 1mW laser was modulated at a frequency of 10 kHz, and the output of the InGaAs PIN photodiode was sent to a lock-in amplifier (SRS SR-530) which was referenced to this modulation.

The x and y step sizes were chosen as 100 micron and 125 micron respectively. The metal surface and the image are shown in Figure 4.13. As it is seen above, roughness that specifies boundaries of the letter "A" is distinctive although the resolution value was restricted by a long step size of 125 micron.
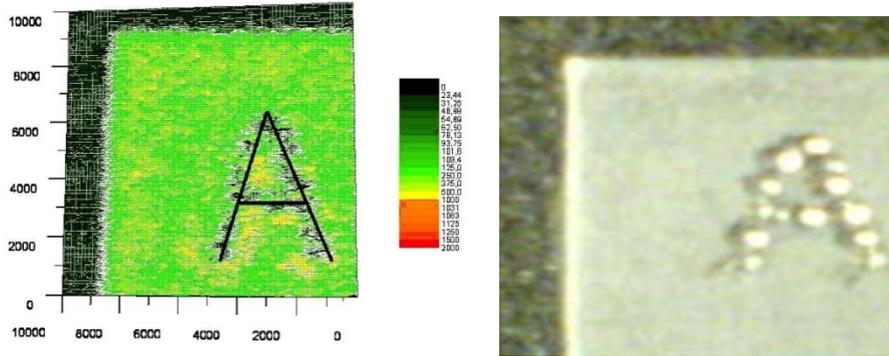
Figure 4.13 The image obtained by the wide field imaging system (left), and the surface that was viewed (right)

To test the axial resolution of these imaging methods, a confocal imaging system had to be built. As was shown in Chapter 3, with a confocal imaging system, features along the axial direction can be discerned. For the gun barrel imaging, the system shown in Figure 4.12 was planned to be built.

The minimum half-spot size of that confocal system will be exactly the radius of the focused beam spot, and the radial resolution will be given by the Rayleigh criterion as was mentioned before. In the confocal system, the distance from the fiber exit to the lens, with a magnification, $M = 1$, and the distance from the lens to the surface of the metal object were both 4.4 mm. The spot size of the beam can be calculated from the formula [42];

$$\omega^2 = \omega_0^2 \frac{f^2}{z_0^2 + (d_1 - f)^2} \tag{4.4.2}$$

where d_1 is the distance from the fiber exit to the lens, 4.4 mm, f is the focal length of the lens, 2.24 mm; λ is the wavelength of the source, 808 nm; ω_0 is the minimum beam radius, i.e., beam radius at the fiber exit, 12.5 μm; ω is the beam radius at the

surface of the metal object, and z_0 is the confocal beam parameter and is equal to 0.61 mm according to the following formula [39];

$$z_0 = \frac{\pi \omega_0^{\,2}}{\lambda}$$

(4.4.3)

The spot size of the beam at the surface of the metal object is then calculated as 25 μm. 12.5 μm, half of this value, is the minimum half-spot size that can be obtained from such a system. Using Rayleigh criterion: that the minimum distance between two observable points is given by the dip in intensity of those two points of 26%, the minimum radial resolution is calculated to be 2 x 4.85 μm = 9.70 μm.

4.5 Results and Discussion

The aim of this chapter was to build an imaging system that can be used to measure the inner surfaces of rifled gun barrels. Fiber optics provides convenience in accessing otherwise inaccessible areas of the target objects to be imaged. Two imaging systems were designed, one is a wide field system, and one is a confocal system, to be located in a mechanical construction which is compatible with both imaging systems.

The measurement performed by the wide field system resulted in an image, on which the boundaries of the defects on the metal object could be distinctive, even with large size of scanning steps.

The theoretical radial resolution value was calculated by taking the fact that the beam displays a pure Gaussian pattern into account. Therefore the resolution formulae mentioned in Chapter 2 were not valid for such beam profiles. So, the spot size was calculated first and from this value the radial resolution value of this system was assessed due to the Rayleigh criterion. For the focused beam spot size in the wide-field system, the theoretical value of the spot size was about 20 microns (about 8 micron radial resolution), and if required, this value could be reduced by changing the optical parameters. For comparison if the system used a point source the radial

resolution calculated from equation (2.4.2) will give 4.7 μm. Since the system construction was based on wide field imaging technique, axial resolution could not be assessed.

To obtain an axial resolution, i.e., to distinguish two separate points along the z axis, a confocal system had to be designed. After the determination of the design of the confocal system was completed, the resolution values that can be obtained from this system were considered.

In the confocal system, the intensity pattern would be mostly a Gaussian pattern since for the optical parameters we chose the objective lens is under-filled. The illumination of the source under-filled the objective lens, thus, it was focused to a beam waist that is Gaussian in cross section. Similarly with the wide field system, the radial resolution was calculated from the spot size of this system, and it was found that the radial resolution is 9.7 micron. This value is not much undesirable, since our goal was to image the inner surface of the gun barrel with a 0,01mm precision. It is possible to improve this limit it by changing the optics and optical parameters. For comparison if the system used a point source the radial resolution calculated from equation (2.5.1) will give 0.63 μm. This shows that under-filling the lens results in a loss of resolution.

Calculation of the axial resolution would be much easier if the lens of the system was overfilled by the source. The axial resolution formula for uniformly illuminated confocal systems is simple and well defined (equation (2.5.2)). The Gaussian beam profile is totally different from the diffraction profile; still, the Rayleigh criterion is valid in considering resolving to separate points along the optical axis [21].

To calculate the resolution in the axial direction, the Gaussian intensity equation can be used. As was mentioned in Section 2.4; according to the Rayleigh limit, there has to be about 20-30% separation between two successful maxima in the intensity pattern to resolve two different points on the object [31]. Starting from this point of view, it is assumed that there is 26% intensity separation between two resolved

points in the along the optical axis. The Gaussian intensity function is the following [21];

$$I(r,z) \propto \exp\left(\frac{-2r^2}{\omega^2}\right) \tag{4.4.4}$$

where r and z are the radial and axial parameters respectively, and ω is a function of z, defined by [43];

$$\omega(z) = \omega_0 \sqrt{1 + \left(\frac{z}{z_0}\right)^2} \tag{4.4.5}$$

ω_0 is the minimum beam radius, i.e., the beam radius at $z = 0$, and z_0 is the confocal beam parameter defined in equation (4.4.3). The intensity difference between two resolved points along the optical axis has to be 26%. At $r = \omega_0$, the intensity of the beam is 86 percent of the maximum intensity. The point that will give the minimum distance to resolve two points along the z axis, then, has to have intensity, 0.74 times the intensity at $z = 0$, which is 86 percent of the maximum intensity. So the beam waist at that point can be defined as;

$$0.86 \times 0.74 = 0.64 \rightarrow 0.36 = \exp\left(\frac{-2\omega_0^2}{\omega^2(z)}\right) \tag{4.4.6}$$

According to above equation the beam waist where the intensity drops %26 percent is calculated as 17.5 μm. Substituting this value into equation (4.4.5), z is found as;

$$z = 595\mu m \tag{4.4.7}$$

This value is the Gaussian limit for the axial resolution of the confocal system described by the parameters mentioned above. In other words a pure Gaussian pattern will display a resolution in the axial direction at most ∼ 0.6 mm in such a configuration. A pure Gaussian pattern means that the beam diameter at the lens is much smaller than the lens diameter. In this case, the beam diameter is smaller than the lens diameter. The results suggest that the intensity pattern of this system is a

mixture of Gaussian and diffraction patterns with the dominance of Gaussian pattern [21], and the Gaussian axial resolution limit is about 0.6 mm. This value is quite large compared with the aimed value, which is 0.01 mm. As was mentioned before, if the illumination was a uniform irradiance, then the resolution parameters (radial and axial resolutions respectively) would be;

$$\Delta r = 0.44 \frac{\lambda}{NA} = 0.63 \mu m$$

$$\Delta z = 1.5 \frac{\lambda}{NA^2} = 3.86 \mu m$$

(4.4.8)

where *NA* is the numerical aperture of the lens (not the fiber), and is equal to 0.56, and wavelength of the source, λ, is 808 nm.

One can optimize by arranging the optical parameters so as to obtain a system in which the source illumination overfills the lens pupil, then it is possible to reduce the axial resolution. In the current confocal system the numerical aperture of the fiber through which the laser illumination passes is 0.15, and it allows the beam diameter to reach to a value of 1.3 mm after traveling a distance of 4.4 mm, where the focusing lens is located. Using a fiber with higher numerical aperture one can allow the beam diameter reaching or exceeding the diameter size of the lens pupil, 2.5 mm. In that case, the source illumination will be a uniform irradiance and therefore the intensity pattern will be a diffraction pattern, providing much smaller resolutions.

The optimum pinhole size was mentioned at the end of Chapter 3 while considering the optimum pinhole size for the Home-Built Confocal Microscope. The objective lens used in the confocal system has a focal length of 2.24 mm and a diameter of 2.5 mm, it corresponds to a numerical aperture (*NA*) of 0.56. The source wavelength is 808 nm and the magnification of the lens is 1. The optimum pinhole size can, then, be calculated as;

$$D_{opt.} = 3M \frac{0.44\lambda}{NA} = 1.9 \mu m$$

(4.4.8)

61

which agrees with the values listed in equation (4.4.8). The actual pinhole size, i.e., the diameter of the fiber exit is 25 micron, so that the optimum value is about 1/13 of the actual value. To optimize the system, either a lens with more magnification or a fiber with a smaller core can be used. The more magnification, the smaller the spot size of the beam; thus, increasing the magnification can improve the radial resolution. To choose a source with smaller wavelength can also be an option.

The optimization of the system requires a careful investigation, including performing experiments with various optics. In the near future this system will be built due to the theoretical results mentioned up to now, and images will be analyzed. And if necessary the optics will be changed with the ones having optimum parameters.

CHAPTER 5

CONCLUSIONS

This study focused on the development of an all-fiber laser scanning confocal imaging system to be used in the analysis of the surfaces of rifled gun barrels and/or metal pipes with a degree of precision (+/-0.01 mm). Initially, the theoretical background for confocal microscopy with the comparison of wide field microscopes was given. Afterwards a free-space confocal system with a laser source was constructed and tested at a wavelength of 808 nm. To image the inside surface of rifled gun barrels, a mechanical system was designed and constructed. Before the optical system was implemented an all-fiber wide field imaging system was designed and tested at a working wavelength of 1550 nm. Thereafter, a confocal all-fiber optical system at a working wavelength of 808 nm was designed but could not be tested due to the poor axial resolution of the system.

In confocal microscopy since the PSF of a confocal microscope is sharper than the wide field one, it is possible to obtain high contrast images. It was shown that confocal techniques provide images with both lateral and axial resolutions 30 percent lower than the resolutions that can be obtained from a wide field microscope. This analysis is based on the fact that the source of illumination is a point source and is assumed to fill the objective lens. For a laser beam used as a source, the intensity patterns of a uniformly illuminated (over-filled) and under-filled pupil by a Gaussian beam vary in both axes. Under-filled pupils display large resolution parameters, however partially filled pupils results in a pattern of mixture of Gaussian and diffraction patterns. It was shown that by taking the resolution of the imaging system to be defined as the minimum observable distance between two points given by a dip in the intensity of 20-30% (Rayleigh criterion for imaging), an under-filled pupil results in a poor axial and lateral resolution.

To test the working principles of a scanning confocal laser imaging system a free-space optical system at a working wavelength of 808 nm was designed and built in the Terahertz Research Laboratory in the Physics department at Middle East Technical University. Measurements indicated that it was possible to obtain both two and three dimensional views of metal surfaces by a system based on confocal technique. The theoretical axial resolution values agreed with the measurements obtained. The radial resolution could not be verified due to the fact that the scanning process was slow and tedious, so that a step larger than the radial resolution was used in the lateral directions.

Then, it was found that the pinhole has a great significance in confocal systems, since the optical instrument that makes possible to resolve two separate points on a plane longitudinal to the optical axis is the pinhole. The larger the pinhole, the more photons pass through it, but, also the less selection of focal volume among scattered light, i.e., the more photons reflected back from the out of focus points are collected. The pinhole sizes used in the measurements were comparable with the calculated value of about 40 microns as given in Chapter 3. Specifically, the 20 micron diameter pinhole was able to collect less intense light so that the images were dim compared to ones obtained by the 100 micron diameter pinhole. However, the 20 micron diameter pinhole displays a decrease in contrast with even small distances away from the focal plane compared to the 100 micron diameter pinhole.

To image the inner surfaces of rifled gun barrels and/or metal pipes the developments of two optical systems based on two different wavelengths, one at 808 nm and one at 1550 nm, was discussed. Both systems are fiber optic systems which, except for the light being guided inside an optical fiber, are very similar to free-space systems. The advantages of a fiber system for confocal imaging is that the fiber core can serve as both a pin-hole in detection and as a means to simulate a point source for the laser beam, a necessary requirement to obtain the minimum resolution patterns for over-filled pupils. Fiber optics provides convenience in accessing otherwise inaccessible areas of the target objects to be imaged.

The measurement performed by the wide field system resulted in an image, on which the boundaries of the defects on the metal object could be distinctive, even with large size of scanning steps. The theoretical radial resolution value was calculated by taking the fact that the beam displays a pure Gaussian pattern into account since the objective lens was under-filled. For the focused beam spot size in the wide-field system, with the optical parameters that were chosen the theoretical value of the spot size was found to be about 20 microns (about 8 micron radial resolution), which agrees with our goal of imaging the surfaces of rifled gun barrels at a resolution of +/-0.01 mm. For comparison if the system used a point source the radial resolution was calculated to be 4.7 μm. Since the system construction was based on wide field imaging technique, axial resolution could not be assessed.

To obtain an axial resolution, i.e., to distinguish two separate points along the z axis, a confocal system was designed. The optical parameters were selected so that the inner surfaces of rifled barrels of 3 distinctive diameters could be imaged, namely: 5.56 mm, 7.62 mm, 9 mm. For the optical system this meant that the image distance from the lens to the metal surface had to be at least 4.5mm (half of the 9mm inner diameter rifled bore). We designed a system that would satisfy both this and the requirement that the images had to be taken at a precision of +/-0.01 mm. Even though the optical parameters were optimized to give a lateral resolution within this limit and at this image distance, the axial resolution turned out to be a problem due to the under-filling of the pupil. Thus, in the confocal system, the intensity pattern would be mostly a Gaussian pattern. The illumination of the source under-filled the objective lens, thus, it was focused to a beam waist that is Gaussian in cross section. Similarly with the wide field system, the radial resolution was calculated from the spot size of this system, and it was found that the radial resolution was 9.7 micron. This value is acceptable since our goal was to image the inner surface of the gun barrel with a +/-0.01 mm precision. For comparison if the system used a point source the radial resolution was calculated to be 0.63 μm. This shows that under-filling the lens results in a loss of lateral resolution. While the lateral resolution was satisfied by our optical design the axial resolution was not. The axial resolution would have agreed if the lens of the system was overfilled by the source. The axial resolution

formula for a uniformly illuminated confocal system is based on the beam diffraction profile (Airy pattern). Although the Gaussian beam profile is totally different from the diffraction profile; still, the Rayleigh criterion is valid in considering resolving to separate points along the optical axis [21].

Using this approach we calculated the axial resolution using Gaussian beam formulae and found that for the optical system we proposed the axial resolution was on the order of 0.6 mm much larger than the precision of +/-0.01 mm which was our goal. As was mentioned in Chapter 2, if the illumination was of a uniform irradiance, then the resolution parameters (radial and axial resolutions respectively) would be;

$$\Delta r = 0.44 \frac{\lambda}{NA} = 0.63 \mu m$$

$$\Delta z = 1.5 \frac{\lambda}{NA^2} = 3.86 \mu m$$

based on the optical parameters of our all-fiber confocal design where NA is the numerical aperture of the lens (not the fiber), and is equal to 0.56, and wavelength of the source, λ, is 808 nm. One can optimize by arranging the optical parameters so as to obtain a system in which the source illumination over-fills the lens pupil, and then it is possible to reduce the axial resolution.

To improve upon these limits changing the location of the fiber with respect to our objective lens so as to over-fill the aperture is not a sufficient parameter to improve the axial resolution. For example after moving the fiber exit of the illumination to a distance of at least twice the focal length of our objective lens we get an improved axial resolution, however our imaging distance has now decreased well below the 4.5mm limit imposed before. Therefore, besides using a point source or over filling the lens, by using a fiber with higher numerical aperture one can allow the beam diameter reaching or exceeding the diameter size of the lens pupil, 2.5 mm. In that case, the source illumination will be a uniform irradiance and therefore the intensity pattern will be a diffraction pattern, providing much smaller resolutions. In addition, to optimize the system, either a lens with more magnification or a fiber with a smaller core can be used. The more magnification, the smaller the spot size of the

66

beam; thus, increasing the magnification can improve the radial resolution. Or choosing a source with smaller wavelength can also be an option.

Finally a mechanical system was designed to house the fiber-based imaging system and the rifled gun barrels and/or metal pipes. The system could accommodate cylindrical objects with lengths of up to 1 m and outer diameters of up to 20 mm. These parameters were adequate to analyze the inner surfaces of the rifled gun barrels whose bore diameters were 5.56, 7.62 and 9 mm.

Before images of the rifled gun barrels can be obtained using the mechanical system that was constructed the optical system needs to be optimized. To achieve an axial resolution of +/-0.01 mm with a laser based illumination our results suggest that a special multi-element objective lens is needed. Work on such a system is planned for the near future.

REFERENCES

[1]   Edward, D. L. (1970). *U. S. Patent No 3,496,667*. New Haven: Olin
        Mathieson Chemical Corporation.

[2]   Gow, J.G., Bloom D. A., & Walsh A. (1998). Harold Hopkins and optical
        systems for urology - an appreciation. *Urology*, 52(1), 152-157.

[3]   Morgenstern, L. (2004). Harold Hopkins (1918-1995): "let there be light...".
        Surgical Innovation, 11(4), 291-292.

[4]   Duchowski, A. A., Gramopadhye, A. K., Sadasivan, S. S., Stringfellow, P. P.,
        & Vembar, D. D. (2005). Design of a virtual borescope: a presence study
        [View Paper]. 367.

[5]   Inanc, F. (2007). A borescope based optical surface scanner. *AIP Conference
        Proceedings*, 894(1), 1715-1722.

[6]   Davidson, M. W., & Abramowitz, M. (2002). Optical microscopy.
        Encyclopedia of Imaging Science and Technology, Vol. II, edited by J.
        Hornak. 1106-1141.

[7]   Rowland, R. E., & Nickless, E. M. (2000). Confocal microscopy opens the
        door to 3-dimensional analysis of cells. *Biosciene*, 3-7.

[8]   Amos, W., White, J., & Fordham, M. (n.d). Use of confocal imaging in the
        study of biological structures. *Applied Optics*, 26(16), 3239-3243.

[9]   Wilson, T. (1999), Principles of three-dimensional imaging in confocal
        microscopes. *Journal of Microscopy*, 193: 91–92.

[10]   Paddock, S. (2000). Principles and practices of laser scanning confocal
        microscopy. *Molecular Biotechnology*, 16(2), 127-149.

[11]   Lundy, T. (2006) Advanced confocal microscopy: an essential technique for microfluidics development. *Microscopy Today*, 8-12.

[12]   Corle T. R., & Kino G. S. (1996). *Confocal Scanning Optical Microscopy and Related Imaging Systems*. New York: Springer.

[13]   Roberts F., & Young J. Z. (1952). The Flying-Spot Microscope. *Proceedings of the IEE - Part IIIA: Television* 99(20), 747-757.

[14]   Roberts F., & Young J. Z. (1951). A Flying-Spot Microscope. *Nature,* 167, 231.

[15]   Minsky M. (1988). Memoir on Inventing the Confocal Scanning Microscope. *Scanning*, 10**,** 128-138.

[16]   Semwogerere D., & Weeks E. R. (2005). Confocal Microscopy. *Biomedical Engineering*, 23(2), 1-10.

[17]   Prasad, V., Semwogerere, D., & Weeks, E. R. (2007). Confocal microscopy of colloids. *Journal of Physics: Condensed Matter*, *19*(11), 113102. IOP Publishing.

[18]   Rafael Leiva-García, José García-Antón and Ma José Muñoz-Portero (2011). Application of confocal laser scanning microscopy to the in-situ and ex-situ study of corrosion processes, *Laser Scanning, Theory and Applications, edited by Chau-Chang Wang.* InTech.

[19]   Carlsson, K., & Åslund N. (1987) Confocal imaging for 3-D digital microscopy. *Appl. Opt.*, (26) 3232-3238.

[20]   Edward, D. L. (1996). *U. S. Patent No 5,532,873.* Ontario: Philips Electronics LTD.

[21]   Webb, R. H. (1996). Confocal optical microscopy. *Rep. Prog. Phys*, 59, 427–471.

[22]   Novotny, L., & Hecht, B. (2006). *Principles of nano-optics*. New York: Cambridge University Press.

[23]   Richards B., & Wolf E. (1959). Electromagnetic diffraction in optical systems II. Structure of the image field in an aplanatic system. *Proc. R. Soc*. A 253, 358-379.

[24]   Kant, R. (n.d). An analytical solution of vector diffraction for focusing optical-systems with seidel aberrations. 1. Spherical-aberration, curvature of field, and distortion. *Journal of Modern Optics*, 40(11), 2293-2310.

[25]   Liu, L., & Tan, H. (n.d). Inverse radiation problem in three-dimensional complicated geometric systems with opaque boundaries. *Journal of Quantitative Spectroscopy & Radiative Transfer*, 68(5), 559-573.

[26]   Paraxial Optics. Alda, J. (2007). *Encyclopedia of optical engineering, edited by Ronald G. Driggers, Craig Hoffman, and Ronald Driggers*. Taylor & Francis.

[27]   Watson G. N. (1922). *A treatise on the theory of Bessel functions*. Cambridge; New York: Cambridge University Press.

[28]   Born, M., & Wolf, E. (1999). *Principles of optics: electromagnetic theory of propagation, interference and diffraction of light*. Cambridge; New York: Cambridge University Press.

[29]   Spring, K. R., Fellers, T. J., & Davidson M. W. *Resolution and contrast in confocal microscopy*. Retrieved August 2011, from http://www.olympusconfocal.com/theory/resolutionintro.html

[30]   Murphy, D. B. (2001). *Fundamentals of light microscopy and electronic imaging, edited by Douglas B. Murphy*. New York: Wiley-Liss.

[31]   Rayleigh criterion. Ridpath, I. (1997). *A dictionary of astronomy, edited by Ian Ridpath*. Oxford; New York: Oxford University Press.

[32]   Claxton, N. S., Fellers, T. J., & Davidson, M. W. (1979). Laser scanning confocal microscopy. *Microscopy*, *1979*(21), 71-82.

[33]   Padgett, M., & Allen, L. (n.d). The poynting vector in Laguerre-Gaussian laser modes. *Optics Communications*, 121(1-3), 36-40.

[34]   James B., P., & Barry R., M. (2008). Handbook of biological confocal microscopy, Third Edition. *Journal of Biomedical Optics*, 13(2), 29902.

[35]   Delaney, P., Harris, M., & King, R. (1994). Fiber-optic laser scanning confocal microscope suitable for fluorescence imaging. *Applied Optics*, 33(4), 573-577.

[36]   Pawley, J. B., Blouke, M. M., & Janesick, J. R. (1996). CCDiode: an optimal detector for laser confocal microscopes. *Proc. SPIE* 2655, 125-129.

[37]   Mason, W. T. (1993). *Fluorescent and luminescent probes for biological activity: A practical guide to technology for quantitative real-time analysis.* London: Academic Press.

[38]   Rosen, J. H. (1972). *Diffraction patterns produced by focused laser beams.* Santa Monica, Calif: Rand.

[39]   *Aluminum Structural Framing.* Retrieved August 25, 2011, from http://www.boschrexroth-us.com/country_units/america/united_states/sub_websites/brus_dcl/Products/Aluminum_Structural_Framing/index.jsp

[40]   Xi, P., Rajwa, B., Jones, J. T., & Robinson, P. (2007). The design and construction of a cost-efficient confocal laser scanning microscope. *American Journal of Physics*, 75(3), 203-207.

[41]   Self, S. (1983). Focusing of spherical Gaussian beams. *Applied Optics*, 22(5), 658-661.

[42]   Yariv, A., & Yeh, P. (2007). *Photonics: Optical electronics in modern communications.* New York: Oxford University Press.

[43]   Saleh, B. E. A., & Teich, M. C. (1991). *Fundamentals of photonics*. New York: John Wiley & Sons.

[44]   Abramowitz, M., & Stegun, I. A. (1964). *Handbook of mathematical functions with formulas, graphs, and mathematical tables, edited by Milton Abramowitz and Irene A. Stegun*. Washington, U.S. Govt. Print. Off.

APPENDIX A

PLOT OF THE POINT SPREAD FUNCTION

It is useful to examine the details on how to construct the basic code of the point spread function given in equation (2.3.9).

i.   It is expected that the greater upper limit of the index of the summation is chosen, the more correct result is taken, i.e., the function is indeed goes to infinity in the equation. Yet, some of the MATLAB codes which has been run with different limits of the summation functions in equation (2.3.9) results with some unwanted spaces in the graph. As seen in Figure A, increasing the upper limit for the summation function causes more spaces show off in the graph. The reason for this, however, is the zeroes of the Bessel function. As the upper limit for the summation function goes to infinity, more Bessel zeroes coincide with u-v range, and as a result, Lommel functions U_1 and U_2 in equation (2.3.9) become undefined near the values close to zero for u and v [44].

ii. Limits of the independent parameters u and v has been chosen such as the ratio of them does not exceed the value 3. The reason for this choice is to avoid unexpected peaks in the boundaries causing by the dominance of $\left(\frac{u}{v}\right)^{n+2s}$ factor in the Lommel functions.

iii. If the argument is real and negative, Bessel function returns a complex number. Therefore the absolute values of the Lommel functions have been taken instead of themselves.
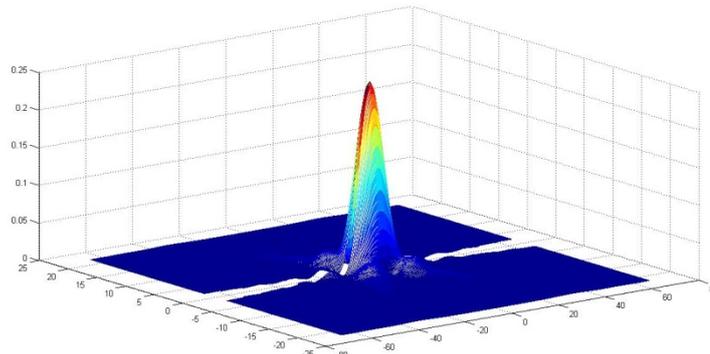
a) *Graph of the point spread function when the upper limit of the index parameter of the summation function is taken 100.*
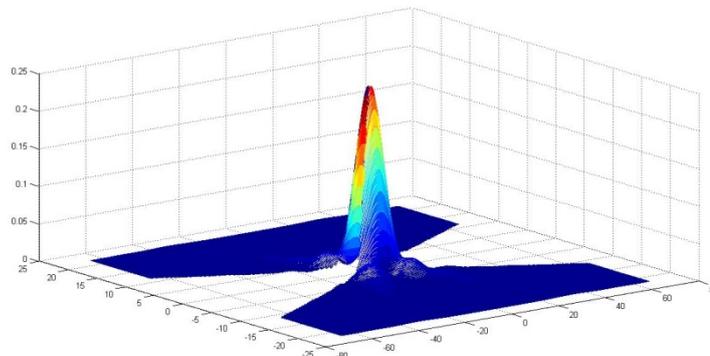
b) *Graph of the point spread function when the upper limit of the index parameter of the summation function is taken 200.*
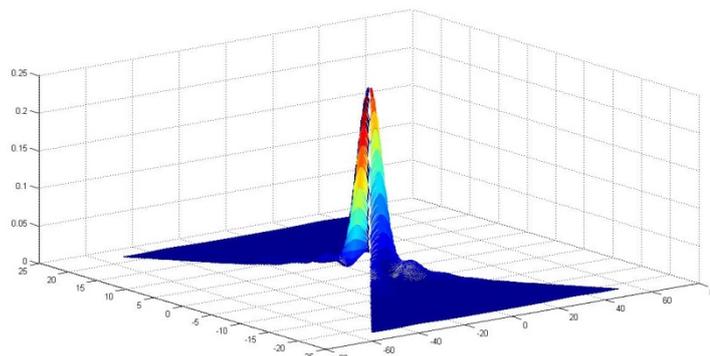
c) *Graph of the point spread function when the upper limit of the index parameter of the summation function is taken 400.*

Figure A Graphs of the equation (2.3.9) with different limits of the summation

function

iv.   A further considerable issue related with the frequency of the points in *u*-range. When the mesh-grid of the parameter *u* has been chosen in such a way that there is not adequate number of points, there appears a space through $v = 0$ axis. However, when the frequency is increased enough (for instance 0.01) this problem is removed.

The function in equation (2.3.9) has been plotted in MATLAB by using the code above;

```
1    [u,v] = meshgrid(-21*pi:.25:21*pi, -7*pi:.25:7*pi);
2    U1 = 0;
3    U2 = 0;
4    for s = 0:50;
5    U1dummy = (((-1)^s).*((u./v).^(1+2*s)).*(besselj((1+2*s),v)));
6    U1 = U1 + U1dummy;
7    U2dummy = (((-1)^s).*((u./v).^(2+2*s)).*(besselj((2+2*s),v)));
8    U2 = U2 + U2dummy;
9    end
10   w = (1./u.^2).*((abs(U1).^2)+(abs(U2).^2));
11   mesh(u,v,w)
```

The most reasonable graph is obtained when 50 is chosen for the upper limit of the summation (Figure A).